



# Sensitivity analysis of BISON model for characterization of impact of experimental parameters on hydrogen migration and redistribution in zirconium-based alloys

Seok Bin Seo<sup>a</sup>, Edward Matthew Duchnowski<sup>a</sup>, Miles O'Neal<sup>a</sup>, Arthur T. Motta<sup>b</sup>, Florian Passelaigue<sup>b</sup>, Soyoung Kang<sup>b</sup>, Giovanni Pastore<sup>a</sup>, Annalisa Manera<sup>c</sup>, Victor Petrov<sup>c</sup>, Pei-Hsun Huang<sup>c</sup>, Nicholas R. Brown<sup>a,\*</sup>

<sup>a</sup> University of Tennessee, Knoxville, TN, USA

<sup>b</sup> Penn State University, State College, PA, USA

<sup>c</sup> University of Michigan, Ann Arbor, MI, USA



## ARTICLE INFO

### Article history:

Received 8 January 2021

Revised 26 February 2021

Accepted 10 March 2021

Available online 15 March 2021

### Keyword:

Hydrogen migration  
Hydrogen redistribution  
Hydride embrittlement  
Zirconium-based cladding  
BISON code  
Sobol sensitivity analysis

## ABSTRACT

The formation of hydrides, a result from excess hydrogen uptake by the cladding during nuclear reactor operation, can significantly impact cladding integrity. We present a sensitivity and uncertainty analysis of a hydrogen predictive model in the BISON fuel performance code to characterize the key input parameters involved in the model. This includes identifying the key parameters necessary to simulate hydrogen behavior in the fuel cladding, revealing the impact of environmental conditions on hydrogen distribution, and informing the envelope of conditions for ongoing experimental work conducted by the University of Michigan. The Sobol sensitivity analysis reveals the quantitative impacts of environmental conditions on the predicted total hydrogen concentration, as well as the respective impact on their sensitivity with respect to the physical parameters. Overall, the precipitation of hydrogen that occurred at the cold end of the sample is the most important phenomenon in the prediction of hydrogen concentration. The optimization study using the results from sensitivity analysis indicates that the BISON simulations produce accurate hydrogen predictions when the sets of parametric ranges are shifted to enable more precipitation to occur at the cold end. Lastly, the sensitivity and uncertainty (S/U) analysis for the ongoing benchmarking experiments supports the focus of experiments that lies on the measurement of Soret effect of hydrogen driven by linear temperature gradients. The outputs are expected to better characterize the various parameters involved in the hydrogen transport model in the BISON code, and improve the understanding of the hydrogen transport behaviors in zirconium-based fuel cladding in a range of expected environmental conditions.

© 2021 Elsevier B.V. All rights reserved.

## 1. Introduction

Nuclear fuel cladding is a primary safety barrier in a nuclear reactor that helps prevent leakage of radioactive fission products into the reactor cooling circuit during an abnormal event. Existing nuclear reactors extensively use zirconium alloys as a nuclear fuel cladding material because of low neutron absorption cross section, good thermal conductivity, dimensional stability, and corrosion resistance [1]. Although zirconium alloys have good high temperature corrosion resistance, continuous exposure to the coolant water causes a slow corrosion of the outer surface of the fuel cladding

and the associated hydrogen ingress into the zirconium cladding during normal reactor operation [2]. The formation of hydrides resulting from the excess of hydrogen concentration can significantly affect cladding integrity by reducing the cladding ductility during normal operation [3], which may cause the failure of cladding in reactivity-initiated accidents (RIAs) [4]. Furthermore, absorbed hydrogen in the cladding affects the kinetics of crystallographic phase transformation of zirconium alloys during high temperature transients such as a postulated loss of coolant accident (LOCA) [5]. The ongoing research project initiated experimental work to evaluate the physical parameters involved in the hydrogen migration phenomenon as well as modeling work to predict the hydrogen distribution inside the cladding in this context. The experimental program conducted by the University of Michigan aims to design and

\* Corresponding author.

E-mail address: [nbrown49@utk.edu](mailto:nbrown49@utk.edu) (N.R. Brown).

conduct experiments to determine the value of the heat of transport and validate the hydrogen transport model implemented in the BISON code. The modeling program presented here aims at identifying the key parameters for the accurate simulation of hydrogen behavior in the fuel cladding, revealing the impacts of environmental conditions on the prediction of hydrogen behavior, and providing the appropriate envelope of conditions to inform ongoing experimental works. The outputs are expected to improve the overall understanding of hydrogen behaviors. The unique contribution of this paper is the use of Sobol sensitivity measures to characterize the key input parameters involved in the model to predict the resulting hydrogen distribution.

During nuclear reactor operation, the zirconium alloy cladding exposed to the coolant water forms a layer of zirconium dioxide in a chemical reaction with the water:



Some of the hydrogen produced is absorbed by the zirconium alloy [6], as the hydrogen is relatively stable in the  $\alpha$ -phase of the zirconium alloy matrix [7]. Other minor sources, e.g. the radiolytic decomposition of water, also generate hydrogen which partly enters the cladding, although the main contributor is the hydrogen from corrosion [8]. Hydrogen pickup results in a gradual accumulation of hydrogen in the zirconium fuel cladding. Once inside the zirconium alloy cladding, gradients in concentration, temperature, and stress can drive hydrogen migration [9]. When the hydrogen solubility limit in the cladding is exceeded, zirconium hydrides will precipitate in the form of platelets, layers, or a rim near the outer surface of the cladding [10,11]. The presence of these hydrides, predominantly oriented in the circumferential direction, can significantly degrade the cladding fracture toughness and tensile ductility. This causes cladding embrittlement which is a potential life-limiting deterioration mechanism for the nuclear fuel cladding in LWRs [3,12]. Hence, understanding hydrogen distribution and its behavior in zirconium-based fuel cladding is crucial for predicting fuel performance and safety.

Two main mechanisms control the hydrogen migration and redistribution in the zirconium fuel cladding: diffusion of hydrogen in solid solution driven by concentration, temperature and stress gradients, and the precipitation and dissolution of hydride particles. These mechanisms are described in detail in [Section 2.1](#). The respective processes are strongly dependent on the specific properties of hydrogen in zirconium alloys such as solubility, diffusion parameters, etc., as well as the operational conditions such as the total amount of hydrogen ingress into the cladding, temperature profile, and the fuel residence time in reactor core. While specific properties related to hydrogen migration and redistribution in zirconium alloys have been extensively studied [9,13], the mechanistic understanding of the environmental conditions that impact hydrogen behaviors in the zirconium-based fuel cladding is still incomplete.

The total amount of hydrogen absorbed by the cladding, which is equivalent to the total amount of hydrogen involved in the migration and redistribution in the cladding, is one of the most important factors that determine the hydrogen distribution inside the cladding. Morozumi et al. [14] experimentally tested the redistribution of hydrogen in zirconium specimen with various initial hydrogen concentrations. They reported the initial hydrogen concentration affected the location where the hydride was formed as well as the time when the steady-state was reached. These are factors that contribute to the distribution of hydrogen. Kammenzind et al. [15] conducted a large number of experiments under various initial conditions, and reported the initial hydrogen concentration impacted the redistributed hydrogen as well as the measured diffusion parameters. It was obvious that larger initial hydrogen amount produced more hydrides over broader area of the specimen, but

the amount of hydrides did not increase linearly with respect to the initial hydrogen content. How initial hydrogen amount is correlated with the prediction of hydrogen distribution and physical parameters involved in the model is not fully understood.

Hydrogen redistribution in cladding, often leading to hydride precipitation, is governed by the temperature environment; the temperature gradient drives the thermal diffusion of hydrogen and the precipitation and dissolution of hydride occur when the hydrogen concentration exceeds the solubility limit. The hydrogen diffusion driven by a temperature gradient, called the Soret effect, was first observed in zirconium by Sawatzky [16,17] and many studies [14,15,18–23] have confirmed its existence. While most studies [16–18,23] used one specific temperature gradient condition for each to observe thermal diffusion of hydrogen, some presented distinct hydrogen behaviors under various sets of constant temperature gradients. Morozumi et al. [14] reported different values of heat of transport and distinct hydrogen distributions under three different sets of temperature gradients. Kammenzind et al. [15] also noticed the amounts of hydrides formed at the cold end differed in various sets of temperature gradient conditions. Many studies have assumed the heat of transport to be constant, but there are indications that they may vary depending upon the temperature range and gradient [14,15,17,20]. Furthermore, the solubility of hydrogen in the alloy, referred to as a terminal solid solubility (TSS), varies exponentially with temperature [9,11,24–30] from less than 1 wt. ppm at room temperature, up to 300 wt. ppm at high temperature of about 370 °C.

Lastly, the annealing time, which represents the fuel residence time in the reactor core, is of great interest in this paper as well. Sugisaki et al. [18] revealed the distinct hydrogen distributions in the zirconium specimen from a series of experiments under three different annealing time conditions. Hong et al. [23] measured hydrogen distributions in Zircaloy-4 and modified Zircaloy-4 specimens annealed under a constant temperature gradient with two different time conditions. They noted that the hydrogen distribution in the sample became steeper as it was annealed longer, but did not provide any explanation of the impact of the annealing time on the hydrogen behaviors. Nagase [31] carried out experiments using hydrided but unirradiated Zircaloy-4 cladding tubes under rapid heating conditions, annealed for a holding time in range of 0–3600 s. The study presented the radial distribution and morphology of hydrides change depending on the temperature and holding time above a certain temperature, but could not distinguish the respective contributions of temperature and annealing time.

The work presented here aims to better characterize the various parameters involved in the hydrogen transport model implemented into BISON code, and improve the understanding of the hydrogen transport behaviors in zirconium-based fuel cladding under possible environmental conditions. The present paper includes sensitivity and uncertainty analysis of hydrogen transport model under linear temperature gradients which are expected to be given during the normal reactor operation. Typically, different temperature gradients in the axial, radial, and azimuthal directions exist in the fuel cladding during the reactor operation. Therefore, the hydrogen distribution driven by those gradients becomes inhomogeneous which results in the local high concentration of hydride. In particular, a radial hydride distribution observed in fuel cladding exposed to the LWR environment is highly concentrated near the outer edge of the cladding where the temperature is the lowest [32]. Targeting the predicted hydrogen at the coldest end of the sample, Zineb et al. [33,34] verified and validated the comprehensive model of hydrogen migration and redistribution, which was implemented in BISON code, and quantified the impact of uncertainty of the physical parameters of the model. Extended from these studies, this paper presents the quantified impacts of the en-

vironmental conditions on the prediction as well as the parameters using the existing hydrogen transport models [35], and establishes a framework for further analysis using improved model [36]. This sensitivity analysis (SA) technique is further used to support the ongoing experimental program from the University of Michigan, by providing insights in the design of experiments, calibrating the experimental data, and verifying the adequacy of the experiments.

The organization of the remainder of this paper is as follows. **Section 2** presents an overview of the background of hydrogen migration and redistribution models and of historic experiments benchmarked for this study. **Section 3** describes the methodology used to model the hydrogen behaviors in the zirconium cladding and to analyze the impacts of input parameters on the prediction of hydrogen. **Section 4** presents sensitivity and uncertainty analysis of the hydrogen transport models for historic and ongoing experiments. The results from sensitivity and uncertainty analysis inform the key parameters to be used for the optimization study. **Section 5** presents a summary and conclusions.

## 2. Background

### 2.1. Hydrogen migration and redistribution model

The existing model to elucidate hydrogen migration and redistribution in the zirconium alloy fuel cladding includes two principal physical phenomena: hydrogen diffusion in the solid solution in the zirconium-based alloy and hydride precipitation and dissolution. When in solid solution hydrogen diffuses driven by the concentration gradient according to Fick's law,  $J_{\text{Fick}}$  [37], and the temperature gradient called the Soret effect,  $J_{\text{Soret}}$  [16]. The total hydrogen flux  $J_{\text{tot}}$  is the sum of each contribution given by

$$J_{\text{tot}} = J_{\text{Fick}} + J_{\text{Soret}} = -D_H \nabla C_{\text{SS}} - \frac{D_H C_{\text{SS}} Q^*}{RT^2} \nabla T \quad (2)$$

where  $C_{\text{SS}}$  is the hydrogen concentration in solid solution in the zirconium alloy matrix,  $Q^*$  is the heat of transport,  $D_H$  is the hydrogen diffusion coefficient in zirconium-based cladding,  $R$  is the ideal gas constant, and  $T$  is the temperature.

Although the local stress state in the cladding affects the distribution of dissolved hydrogen in a way of influencing migration [38] or solubility limit [39], current model in BISON does not include the effect of stress for the following reasons:

- the BISON model was initially developed based on experimental observations for the evolution of the hydrides from the conditions in the cladding throughout the lifecycle of the fuel rod where the hydrides preferentially precipitate in the circumferential direction and thus rarely cause any cracking behaviors [35,40],
- the effect of stress on solubility, related to the delayed hydride cracking (DHC) [41], has been reported in the literature [42]. However, the level of stress and stress gradient required in such circumstances is much higher than would be expected in our experiments in which no external stress was applied,
- the stress-driven movement of hydrogen was observed when a flaw or notch-tip is present in the sample [43], while the experiments referred to in this paper were conducted under a stress-free environment where no flaws were allowed.

The diffusion coefficient of hydrogen in zirconium follows Arrhenius' law [11,16,44,45]:

$$D_H = A_D \exp\left(-\frac{E_D}{RT}\right) \quad (3)$$

where  $A_D$  is a pre-exponential factor in units of  $\text{m}^2/\text{s}$ ,  $E_D$  is the activation energy for diffusion of hydrogen in zirconium-based cladding in  $\text{J/mol}$ , and  $T$  is the temperature in Kelvin.

Once the concentration of hydrogen exceeds the solubility limit in the alloy, zirconium hydride particles precipitate out of solution, mostly observed as FCC delta hydrides  $\text{ZrH}_{1.66}$  [40]. The volume fraction of hydrides formed depends on the total concentration of hydrogen in the alloy and the alloy's TSS for hydrogen. Previous studies [24,26,28–30] indicated that the terminal solid solubility for dissolution ( $\text{TSS}_d$ ) was different from that for precipitation ( $\text{TSS}_p$ ), while both were described by the Arrhenius formula:

$$\text{TSS}_p = A_p \exp\left(-\frac{E_p}{T}\right) \quad (4)$$

$$\text{TSS}_d = A_d \exp\left(-\frac{E_d}{T}\right) \quad (5)$$

where  $A_p$  and  $A_d$  are pre-exponential factors in wt ppm,  $E_p$  and  $E_d$  are the activation energies in  $\text{J/mol}$  for  $\text{TSS}_p$  and  $\text{TSS}_d$ , respectively.

In those studies the transient behavior of hydrogen in supersaturated and undersaturated solid solution, the rate of precipitation and dissolution  $S$  were accounted for by modeling a kinetic equation [46] in which the constants are determined empirically and follow an Arrhenius law:

$$C_{\text{SS}} > \text{TSS}_p \rightarrow S = \alpha^2 (C_{\text{SS}} - \text{TSS}_p), \quad \text{where } \alpha = A_\alpha \exp\left(\frac{E_\alpha}{RT}\right) \quad (6)$$

$$\text{TSS}_p \geq C_{\text{SS}} > \text{TSS}_d \rightarrow S = 0 \quad (7)$$

$$\text{TSS}_d \geq C_{\text{SS}} \rightarrow S = \beta^2 (C_{\text{SS}} - \text{TSS}_d), \quad \text{where } \beta = A_\beta \exp\left(\frac{E_\beta}{RT}\right) \gg \alpha \quad (8)$$

where  $\alpha$  and  $\beta$  are precipitation and dissolution kinetic parameters, respectively,  $A_\alpha$  and  $A_\beta$  are pre-exponential factors with units of  $\text{s}^{1/2}$ ,  $E_\alpha$  and  $E_\beta$  are the activation energies in  $\text{J/mol}$ .

However, a recent study by Lacroix et al. [36] brought an improved understanding of the physics that hydride precipitation was divided into nucleation of new hydrides and growth of existing ones. According to a new model, called Hydride Nucleation-Growth-Dissolution (HNGD) model, the nucleation of new hydrides occurs when the hydrogen content in solid solution is above the supersolubility limit (equivalent to  $\text{TSS}_p$ ), and the growth of existing hydrides occurs when the hydrogen content in solid solution is above thermodynamic solubility limit (equivalent to  $\text{TSS}_d$ ). The dissolution of hydrides happens below  $\text{TSS}_d$  and is no longer considered instantaneous. These mechanisms occur at specific rates, determined by kinetic parameters, as defined in Eqs. (9)–(11).

$$\text{Dissolution : } \frac{\partial C_{\text{SS}}}{\partial t} = -K_D (C_{\text{SS}} - \text{TSS}_d) \quad (9)$$

$$\text{Nucleation : } \frac{\partial C_{\text{SS}}}{\partial t} = -K_N (C_{\text{SS}} - \text{TSS}_p) \quad (10)$$

$$\text{Growth : } \frac{\partial C_{\text{SS}}}{\partial t} = -K_G (C_{\text{tot}} - \text{TSS}_d) p (1-x) (-\ln(1-x))^{1-1/p} \quad (11)$$

where  $K_D$ ,  $K_N$ , and  $K_G$  are the kinetic parameters for dissolution, nucleation and growth in unit of  $\text{s}^{-1}$ , respectively,  $x$  is a measure of the advancement of the precipitation reaction, and  $p$  is the dimensionality of the growth.

Finally, the differential equations for the evolution of hydrogen concentration in solid solution and for the evolution of the volume fraction of  $\delta\text{-ZrH}_{1.66}$ ,  $V_\delta$  are given by [40]:

$$\frac{\partial V_\alpha C_{\text{SS}}}{\partial t} = -\nabla \cdot V_\alpha J_{\text{tot}} - V_\alpha S, \quad \text{where } V_\alpha \equiv 1 - V_\delta \quad (12)$$

$$\frac{\partial V_\delta}{\partial t} = \frac{M_{ZrH_{1.66}}}{M_H} \frac{V_\alpha S}{1.66} \quad (13)$$

where  $V_\alpha$  is the volume fraction of the  $\alpha$ -Zr phase.

The BISON code uses a clamping factor,  $f_c$  to accurately predict the measured thickness of a hydride rim, a radially localized hydride layer near the outer LWR cladding surface, for cases where the volume fraction of the hydride in the rim is much less than unity [35]. By modifying a clamping factor, BISON allows the user to constrain the maximum allowable volume fraction of hydrides to the maximum hydrogen content possible in a node so that the hydride is likely formed at more nodes, therefore thickening the hydride rim region. Note that the use of clamping factor is restricted to keep  $V_\alpha$  between 0 and 1. Several assumptions made for BISON model are described in the literature [35].

$$V_{\alpha_{\text{apparent}}} = 1 - \frac{V_\delta}{f_c} \quad (14)$$

We should note that the SA study presented in this paper was conducted in parallel with the implementation of the HNGD model in BISON and provided interesting physical insights onto the modeling process as well as associated uncertainties. While the hydrogen evolution and hydride precipitation model used in this work has been superseded recently by a more accurate model in BISON [47], the present study is valid because the prior model still takes into account key mechanisms involved in the migration and precipitation of hydrogen. Future uncertainty quantification (UQ) studies will use the newly implemented model in BISON with a more representative and relevant figure of merit such as the overall fit of the calculated hydrogen distribution over the whole curve.

## 2.2. Benchmarking experiments for hydrogen migration and redistribution model

The experiments of hydrogen diffusion and precipitation discussed in this paper were conducted by Kammenzind and reviewed in a Masters project at Penn State University [48]. In a series of experiments, specimens containing various amounts of hydrogen were annealed under stress-free environments applied various temperature for periods of time ranging from weeks to months in order to approach equilibrium. Initially, the specimens with dimensions of 2.54 cm length, 1.27 cm width, and 0.127 cm thickness were weighed, and placed in a quartz bulb with a pre-weighed amount of zirconium hydride chips. The bulbs containing specimens were vacuumed, sealed, and then annealed at high temperature, allowing the Zircaloy specimen to be homogeneously pre-charged with hydrogen transferred as a gas from the zirconium hydride chips. At the end of the annealing process, the bulbs were quickly cooled to prevent further hydrogen migration, and the initial hydrogen concentration was measured from one of half-sectioned pieces of each specimen.

Once the specimens were pre-charged with hydrogen, they were annealed in a furnace brick with a heat source at the left end and a heat sink at the right end, applying a linear thermal gradient to the specimen. Thermocouples located in four slots of the specimens at distances of 0.089 cm, 0.838 cm, 1.676 cm, and 2.451 cm from the cold end, measured the temperatures of the specimen. The temperature at the cold end was targeted at either 260 °C, 316 °C, 371 °C, or 427 °C, and the temperature gradient was targeted at either 66 °C/cm or 87 °C/cm, which made the hot end temperature 427 °C, 482 °C, 538 °C, 593 °C, 621 °C, or 649 °C. More hot end conditions exist because either temperature gradient was applied independently to the cold end. The annealing time ranged from about ten to eighty days. The pre-charged hydrogen concentration of each specimen was targeted to be below  $TSS_p$  for the lowest specimen temperature so that no hydrides were present at

the start of annealing. After annealing, the specimens were quickly brought to room temperature to fix the hydrogen distribution. The total hydrogen content as a result of hydrogen redistribution and precipitation was analyzed from the sectioned specimens. The details in the experimental setup and process are described in [48].

The ongoing benchmarking experiments have been conducted by the University of Michigan aiming at measuring the value of the heat of transport necessary for the hydrogen migration models in BISON. The experimental procedure is similar to that of Kammenzind's experiment. A sample of ZIRLO material pre-charged with hydrides was subjected to differential heating using two heater cartridges placed at the two opposite sides of the sample creating a linear temperature gradient across the sample. The specimens had dimensions of 4 cm length, 1 cm width, and 0.06 cm thickness. The temperature at the cold end was in the range of 404 – 464 °C, and the temperature gradient was targeted at either ~11 °C/cm or ~30 °C/cm. The annealing time ranged from about five to thirty days. The sample started out with homogeneously distributed hydrides and the temperature gradient caused a variation in the distribution of hydrogen over the sample. After the annealing, the sample was removed from the experiment box and the hydrogen concentration was measured as a function of location by sectioning the sample into small segments. They determined the value of heat of transport by fitting the measured hydrogen profile.

## 3. Methodology

### 3.1. Fuel performance code, BISON

The benchmarking experiments for the hydrogen behaviors were numerically simulated using the fuel performance code BISON. BISON [49] is an engineering-scale fuel performance code based on the finite element method which was developed at Idaho National Laboratory. It can solve the fully-coupled equations of stress equilibrium, heat conduction, and species diffusion for various geometries including 3D solids, 2D plane, and 1D layer [49]. While the modeling capability of BISON originally spans thermal and mechanical behaviors of fuel as well as heat transfer between fuel/cladding/coolant, previous studies implemented a comprehensive model of hydrogen migration and redistribution in the code [35,40]. Recent studies verified several key physics beneath the model [34–36,40], and validated the simulations by comparing them with historic experimental data [33,34,48]. Note that the contribution of stress field to hydrogen migration has not been implemented yet in the BISON code and thus the calculations are valid when no large stress gradients exist.

The physical phenomena considered in the simulations of this paper are the diffusion of hydrogen driven by the concentration gradient and the temperature gradient, and the hydrogen precipitation at the cold end of the specimen. The hydrogen concentration inside the specimen is governed by two different diffusion mechanisms that cause hydrogen to migrate hydrogen in opposite directions. Higher hydrogen concentration at the cold end of the specimen is due to the Soret effect, which then enhances the Fickian diffusion that moves the hydrogen in the opposite direction. According to the model in [35,40], when the hydrogen concentration exceeds  $TSS_p$ , the hydrogen is precipitated as a form of hydride, normally near the cold end. The HNGD model accounting for hydrogen behavior at the hysteresis region has been recently implemented [36,47], but will be dealt with in future work, not in the present paper.

Several assumptions were made to make the BISON code able to simulate the hydrogen behaviors in the historical experiments described in Section 2.2: the temperature gradient was linearly interpolated between thermocouple readings, the total amount of hy-

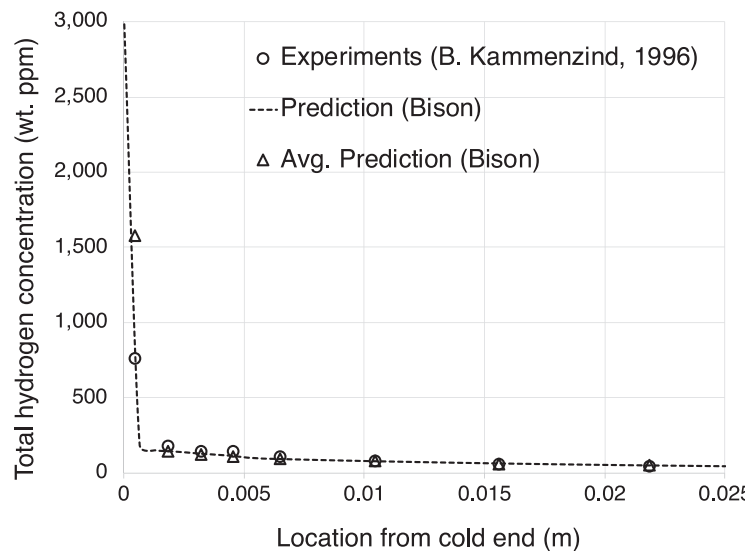


**Fig. 1.** Example of predicted hydrogen distribution by BISON using default values for input parameters.

drogen in the specimen did not change during the calculation, and the hydrogen distribution did not depend on the width or thickness of the specimen (i.e. one-dimensional diffusion was assumed). The 40 mesh elements were split evenly throughout the geometry, initial hydrogen concentration was equally assigned to each element at the beginning of simulations, and the simulations matched the time for the experiment anneals. At each time step, BISON computed the concentrations of soluble hydrogen and zirconium hydrides by solving for diffusion, precipitation rates, dissolution rates, and the time derivatives of hydrogen concentration in solid solution. Then the code used kernels and material properties to evaluate integral values associated with equations in **Section 2.1**, and computed the final hydrogen concentration at each mesh point along the sample. Fig. 1 shows a typical example of hydrogen distribution predicted by BISON code using default input parameters. BISON code predicts the total hydrogen concentration at each node plotted as a dotted line. It clearly shows large hydride precipitation at the cold end. Total hydrogen concentration reported in Kammenzind's experiment was measured from each section of specimen, like the circles in Fig. 1. Therefore, when we compared predicted values to measured values, predicted values were averaged along each length, like the triangles in Fig. 1, that corresponded to that of each section reported in the experiment.

### 3.2. Global sensitivity analysis

A global sensitivity analysis ranks the priority of system inputs which affect the system output [50,51]. This ranking provides a path forward to identifying the most influential input parameters that are responsible for the overall uncertainties of the system, and/or to effectively reducing them. Furthermore, the sensitivity analysis calculates the estimated uncertainties of the specific outputs coupled with those considered for the system inputs. Among various methods, variance-based techniques are commonly used in global sensitivity analyses because of their strengths in computational efficiency and applicability for both linear and non-linear correlation [52]. Sobol sensitivity analysis is one of the variance-based methods that expresses the variance of the output as a finite sum of terms of increasing order [53,54]. In Sobol sensitivity analysis, the first-order term, referred to as the first-order effect, represents the influence of a given input alone and measures the direct impact it has on the output. The higher-order terms repre-

sent the attribution of the variance due to interactions with the other input parameters. This measures the indirect contributions from interactions between different inputs.

Sobol indices for the first-order effect,  $S_i$ , are defined as

$$S_i = \frac{V_{X_i}(E_{X_{-i}}(f(\mathbf{X})|X_i))}{V(f(\mathbf{X}))} \quad (15)$$

where  $\mathbf{X}$  is the matrix of all factors,  $X_i$  is the  $i$ -th factor,  $\mathbf{X}_{-i}$  is the matrix of all factors but  $X_i$ ,  $E(f(\mathbf{X}))$  is the expected value of  $f(\mathbf{X})$ ,  $V(f(\mathbf{X}))$  is the variance of  $f(\mathbf{X})$ , and  $E_{X_{-i}}(f(\mathbf{X})|X_i)$  denotes the mean of  $f(\mathbf{X})$  taken over all possible values of  $\mathbf{X}_{-i}$  while keeping  $X_i$  fixed.

The sum of the variances, referred to as the total effect of the Sobol indices,  $T_i$ , is defined by the following formula:

$$T_i = \frac{E_{X_{-i}}(V_{X_i}(f(X)|\mathbf{X}_{-i}))}{V(f(X))} \quad (16)$$

where  $V(f(X)|\mathbf{X}_{-i})$  denotes the output variance conditional to fixing all the variables except  $X_i$ .

## 4. Results and discussion

### 4.1. Identification of the importance of environmental conditions to hydrogen behaviors

#### 4.1.1. Convergence study

Sobol sensitivity analysis of total hydrogen distributed at the cold end of a specimen for linear temperature gradients was conducted with respect to the integrated set of input parameters. The set of input parameters included model parameters related to the hydrogen migration and redistribution model (e.g. heat of transport, activation energy and pre-exponential factor for diffusion coefficient, activation energy and pre-exponential factor for TSS<sub>p</sub>, activation energy and pre-exponential factor for TSS<sub>d</sub>, activation energy and pre-exponential factor for the precipitation kinetic parameter, hydride clamping factor) and experimental parameters related to the environmental conditions (e.g. cold end temperature, temperature gradient, initial hydrogen content, annealing time). The ranges of model parameters used were taken from the literature, and those of environmental conditions were bounded by experimental knowledge. The input parameters and their respective ranges are listed in Table I.

**Table I**  
Variation ranges for the major input parameters of the Sobol sensitivity analysis.

Parameter	Unit	Lower bound	Upper bound
Heat of transport, $Q^*$	J/mole	25000	50000
Diffusion coefficient: activation energy, $E_D$	J/mole	30000	50000
Diffusion coefficient: pre-exponential factor, $A_D$	$m^2/s$	$10^{-8}$	$10^{-6}$
TSS <sub>p</sub> : activation energy, $E_p$	J/mole	28737	31183
TSS <sub>p</sub> : pre-exponential factor, $A_p$	wt. ppm	124871	152620
TSS <sub>d</sub> : activation energy, $E_d$	J/mole	32183	35782
TSS <sub>d</sub> : pre-exponential factor, $A_d$	wt. ppm	95802	117091
Precipitation kinetic parameter: activation energy, $E_\alpha$	J/mole	37080	45320
Precipitation kinetic parameter: pre-exponential factor, $A_\alpha$	$s^{1/2}$	54	69
Hydride clamping factor, $f_c$	-	0.5	1
Cold end temperature, $T_c$	K	533	644
Temperature gradient, $\Delta T$	K/cm	66.4	88.8
Initial hydrogen content, $C_{ini}$	wt. ppm	37	265
Annealing time, $t_a$	day	6	27

The literature review showed a large scatter in the measurement data of interest for this study. Therefore, we set the range of variation of each input parameter to span measured values reported in the previous studies. For the heat of transport, the variation range was set to 25,000 – 50,000 J/mole to envelop reported values from Sawatzky [17] and Kammenzind et al. [15]. The range of the activation energy of diffusion coefficient of hydrogen in Zircaloy-4 came from 45000 J/mole conducted by Kearns [37] and Kammenzind et al. who found 33000 J/mole [15]. The ranges of variation in activation energies for TSS<sub>p</sub> and TSS<sub>d</sub> were set to about + 15 % from reported values in [55], and those of pre-exponential constants for TSS<sub>p</sub> and TSS<sub>d</sub> were set to about  $\pm 10\%$  from values reported in [30] that were implemented in BISON. The input variables for the precipitation kinetic parameter were varied about  $\pm 10\%$  from the measured value reported in [15]. Note that variation ranges of some input parameters were slightly adjusted to span previously measured values, and we used exact values of each parameter listed in Table I for this study. The variation ranges of environmental parameters were determined to envelop conditions from a set of experiments conducted by Kammenzind [15].

In this study, the predicted total hydrogen concentration at the cold end was chosen as the key Figure of Merit (FoM). Under the linear temperature gradient, the last node at the cold end was the point where the hydrides were most likely to precipitate, and the precipitation produced the largest discrepancy between predicted hydrogen concentration and experimental data (See Fig. 1). The present paper assumed that the total hydrogen concentration at the cold end was representative of the full profile in the accuracy of prediction aspect. To support this assumption, normalized Sobol indices computed for total hydrogen concentration at the cold end and the root-mean-square-error (RMSE) were compared. The normalized Sobol index,  $NT_i$ , was defined as in Eq. (17) to compare Sobol indices computed for different FoMs.

$$NT_i = T_i / \sum T_i \quad (17)$$

The RMSE was calculated for the predicted hydrogen concentration at different positions in the sample compared to the expected experimental data conducted by Kammenzind et al. [15], which was defined as:

$$RMSE = \sqrt{\frac{\sum (Y_{exp} - Y_{pre})^2}{M}} \quad (18)$$

where  $Y_{exp}$  is the expected hydrogen concentration based on the experimental results,  $Y_{pre}$  is the predicted hydrogen concentration by BISON simulation,  $M$  is the number of sections in the sample where the hydrogen content was measured in the experiments. Note that  $Y_{pre}$  was the averaged value for each section corresponding to that in the experiments.

Fig. 2 presents normalized Sobol indices computed for the total hydrogen concentration at the cold end and the RMSE. Note that each notation for corresponding input parameter can be found in Table I. Differences in Sobol indices computed for the hydrogen concentration at the cold end and the RMSE were mostly within 10 %, maximum of 15 % for  $E_p$ , and the rank of respective parameter was found to be same. This indicates that the priority of input parameters as well as the sensitivity of accuracy in prediction of hydrogen distribution remain valid with respect to each parameter, when the total hydrogen concentration at cold end is chosen as FoM. Furthermore, the predicted hydrogen concentration at the cold end as a FoM had its advantage in predicting ongoing experiment where there was no measured data to compare with. Finally, following sensitivity analyses were conducted for the total hydrogen concentration at the cold end as a FoM.

All Sobol indices for the first-order and total effects were evaluated using Saltelli's scheme that extended the Sobol sequence in such a way as to reduce the error rates in the resulting sensitivity index calculations [56]. As a result, the sampler generated a total of  $N \times (2k+2)$  model runs where  $k$  indicates the number of input variables and  $N$  indicates the number of sample size. During the computation process, it was important to determine the sample size needed to obtain reliable Sobol indices, while reducing the overall computational time. The convergence criterion for the sample size is defined by the width of the 95 % confidence intervals for Sobol indices. A value of the width of the confidence interval being close to zero indicated that the Sobol index has converged, and the absolute threshold value of 0.05 was considered to be reasonable for the normalized Sobol indices in the previous studies [57,58].

The convergence study was performed to determine the sample size and assess the convergence of the sensitivity indices. Note that only Sobol indices of model parameters were tested under fixed environmental conditions in order to reduce the number of total runs and consequent computational burden. The width of the 95% confidence intervals for Sobol indices of respective input variables were computed, and the evolutions of Sobol indices and 95% confidence intervals were plotted as a function of the sample size, as shown in Figs. 3 and 4. The Sobol indices show oscillations at smaller sample size but become stable as the sample size is increased. Fig. 4 shows that the width of 95 % confidence level goes below 0.05 at the sample size of 4,000 which is consistent with the point where the Sobol indices have converged. Note that the negative but significantly close to zero value of Sobol index was obtained due to numerical error, though it could be assumed to be zero if the confidence interval was within the convergence criteria [59]. The convergence of Sobol indices representing first order effect was also verified as shown in Figs. 5 and 6. All the following

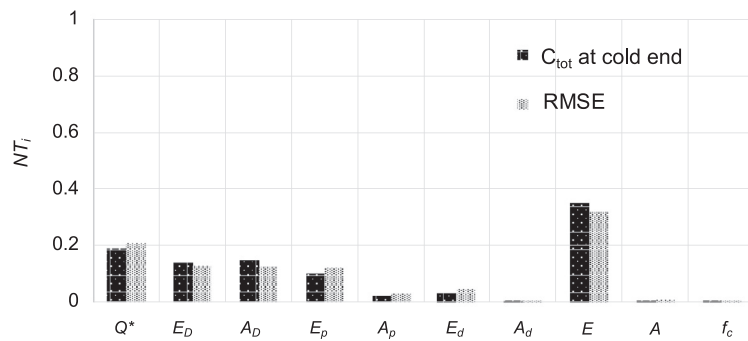


**Fig. 2.** Comparison of normalized Sobol indices of respective parameter computed for predicted total hydrogen concentration at the cold end and the RMSE.

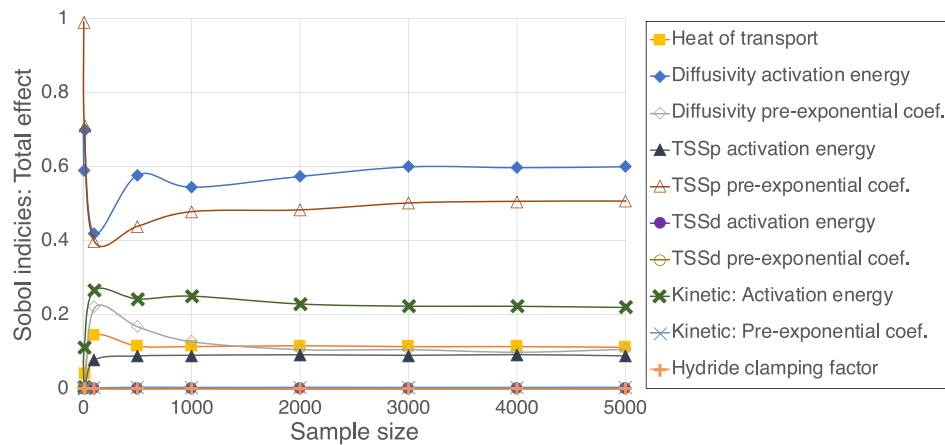


**Fig. 3.** Evolution of Sobol indices for total effect as a function of sample size.

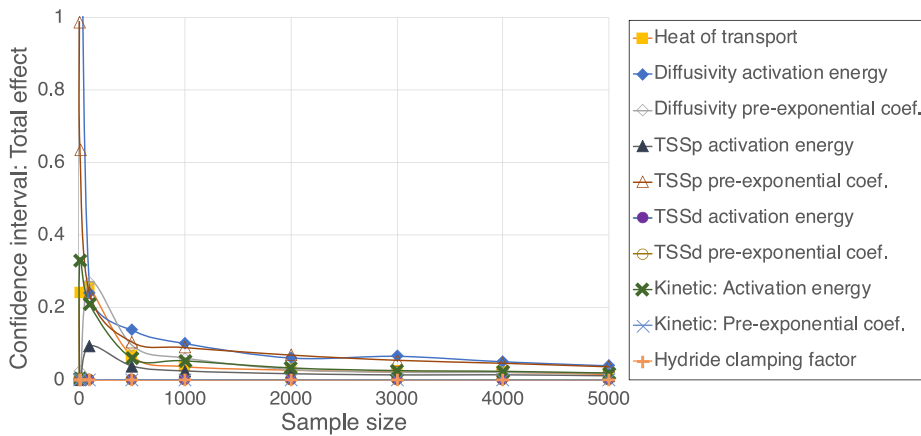


**Fig. 4.** Evolution of 95 % confidence intervals of Sobol indices for total effect as a function of sample size.

analyses in this paper used a sample size of 4,000 for the computation of Sobol indices.

#### 4.1.2. Quantification of effects of environmental conditions

Sobol indices for both the total and first-order effects of inputs on the predicted hydrogen concentration were computed at the cold end under a sharp temperature profile, as shown in Fig. 7. It was found that the initial hydrogen content plays a dominant

role in the prediction of total hydrogen concentration at the cold end. Since the initial hydrogen content directly determined the expected total hydrogen content distributed along the specimen, it was reasonable that the initial hydrogen content gave the largest Sobol indices for total and first order effect. In particular, when the linear temperature profile was applied, the cold end was the point where the hydrogen concentration was the highest and the precipitation more likely happened. The second largest Sobol in-

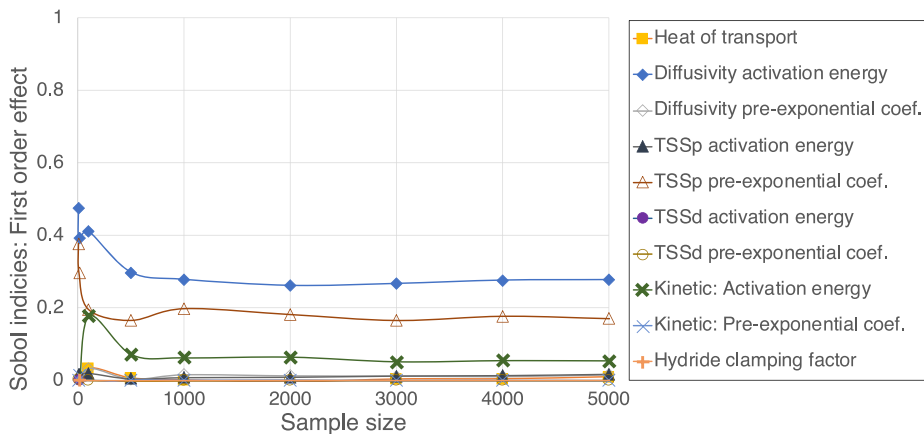


**Fig. 5.** Evolution of Sobol indices for first order effect as a function of sample size.

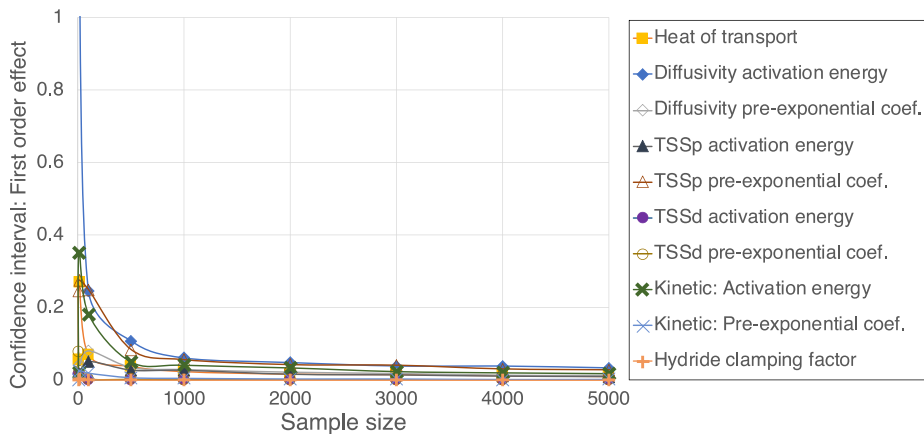


**Fig. 6.** Evolution of 95 % confidence intervals of Sobol indices for total effect as a function of sample size.

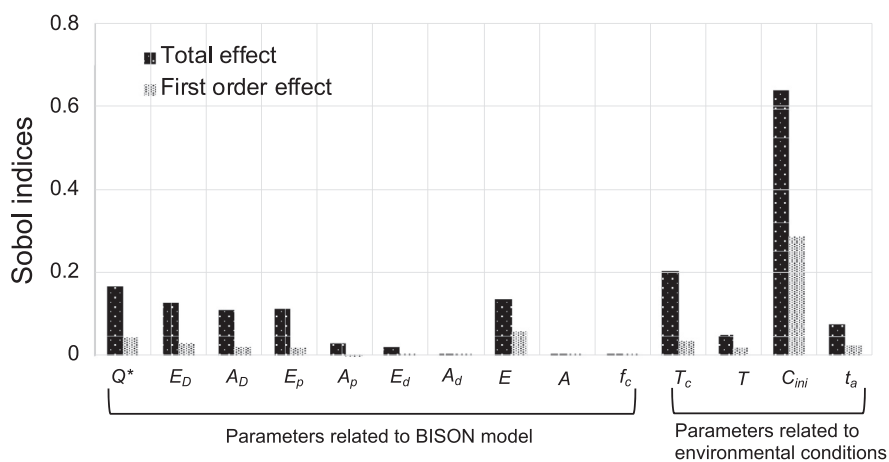


**Fig. 7.** Sobol indices of input parameters for the total hydrogen content at the cold end of specimen.

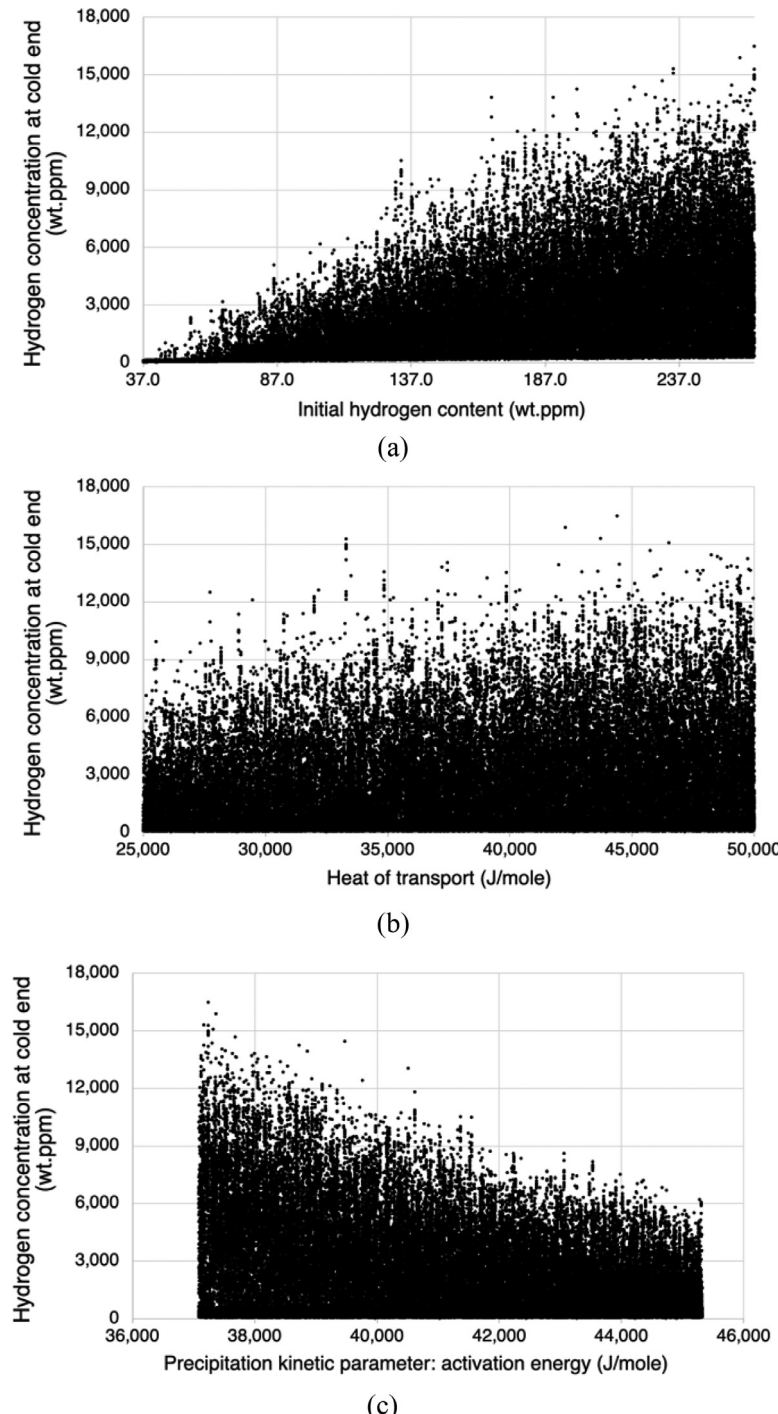


**Fig. 8.** Scatter plot of predicted hydrogen content at cold end with respect to: (a) initial hydrogen content, (b) heat of transport, (c) activation energy for precipitation kinetic parameter.

dex for the first order effect came from the activation energy of the precipitation kinetic parameter,  $E_\alpha$ , which is a direct term in the calculation of the hydride precipitation at the cold end. For the same reason, diffusion parameters ( $E_D$  and  $A_D$ ) give some contributions to the prediction of hydrogen as the sum of first order Sobol indices for  $E_D$  and  $A_D$  is comparable to the sum of precipitation kinetic parameters ( $E_\alpha$  and  $A_\alpha$ ).

Of the parameters related to environmental conditions, the Sobol index for the first order effect of cold end temperature,  $T_c$

was the second largest since it defined the minimum temperature condition along the specimen. The effect of cold end temperature was largely enhanced when it came to total effect showing large interactive effects with most of the other model parameters. This is because the hydrogen behaviors, in particular the diffusion in solid solution and solid solubilities, are highly dependent on the temperature. Note that the Sobol indices for total effect of all the model parameters were largely increased compared to the first order effect, which was a consequence of the complexity and nonlinear-

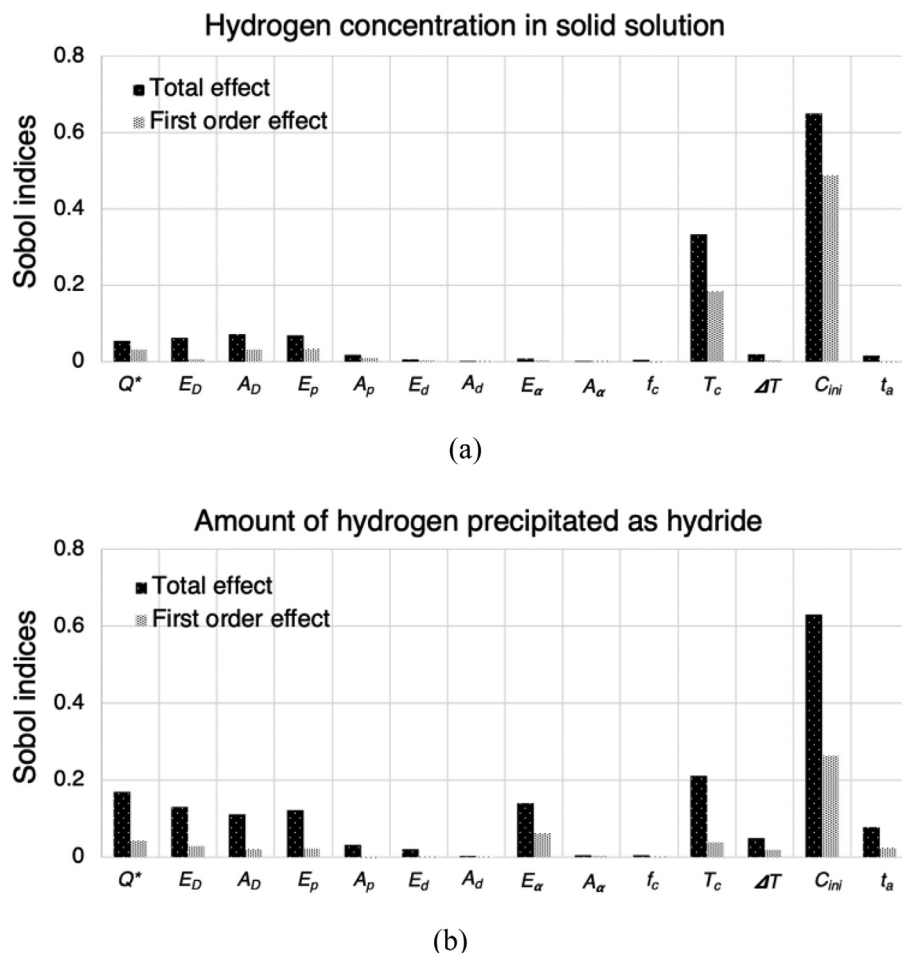


**Fig. 9.** Sobol indices of input parameters for hydrogen prediction at the cold end of specimen: (a) hydrogen concentration in the solid solution, (b) amount of hydrogen precipitated as hydride.

ity of the hydrogen model. Compared to the Sobol indices of cold end temperature, those of temperature gradient,  $\Delta T$  were small. Although the temperature gradient specified the temperature profile along the specimen, it did not affect any other mechanisms included in BISON model except for the hydrogen diffusion driven by Soret effect, thus produced small Sobol indices for total and first order effects. Interestingly, the annealing time had a minor impact on the hydrogen prediction, implying that the steady-state equilibrium in hydrogen migration and redistribution could be reached during any annealing time within the range in this study.

The scatter plots of predicted total hydrogen concentration at the cold end are shown in Fig. 8(a)-(c), with respect to chosen parameters; the initial hydrogen content ( $C_{ini}$ ), the heat of transport ( $Q^*$ ), and the activation energy for the precipitation kinetic parameter ( $E_p$ ). Note that these parameters were chosen because they were found to be the most significant parameters among those related to respective mechanism:  $C_{ini}$  among environmental parameters ( $T_c$ ,  $\Delta T$ ,  $C_{ini}$ ,  $t_a$ ),  $Q^*$  among the diffusion-related parameters ( $Q^*$ ,  $E_D$ ,  $A_D$ ), and  $E_p$  among the precipitation/dissolution-related parameters ( $E_p$ ,  $A_p$ ,  $E_d$ ,  $A_d$ ,  $E_\alpha$ ,  $A_\alpha$ ,  $f_c$ ). Fig. 8(a) presents the predicted hydrogen concentration has a strongly positive correlation with the initial hydrogen content. As the initial hydrogen content increased, the maximum amount of hydrogen that could be precipitated at the cold end increased almost linearly. Furthermore, the predicted hydrogen concentration largely varied as the initial hydrogen content increased. This indicated that the predicted hy-

drogen concentration became more sensitive to the input parameters as total amount of hydrogen content in the sample increased. These results implied that we could predict the maximum amount of hydrogen concentrated at the cold end using the initial hydrogen content along the specimen, but the prediction of the exact value produced a large uncertainty when a large amount of hydrogen was initially charged. Fig. 8(b) presents that large scatters are found over the entire range of the heat of transport, and the predicted hydrogen concentration shows a weak dependency on the heat of transport. This accounted for the large Sobol index for the total effect of the heat of transport with small Sobol index for the first order effect, and represented very strong interactions with other parameters. Thus, the uncertainty in the prediction of hydrogen was effectively reduced only if the estimation of the heat of transport accompanied the accurate measurement of other parameters. The activation energy for the precipitation kinetic parameter presented the strong negative correlation with the precipitated hydrogen at the cold end as shown in Fig. 8(c). This could be described in the same manner as for the initial hydrogen content. The uncertainty in the predicted hydrogen concentration increased with decreasing activation energy for the precipitation kinetic parameter.

Fig. 9(a)-(b) show the computed Sobol indices of input parameters on the predicted hydrogen concentration in solid solution and the amount of hydrogen precipitated as hydride, respectively. For the hydrogen in solid solution, the cold end temperature and the

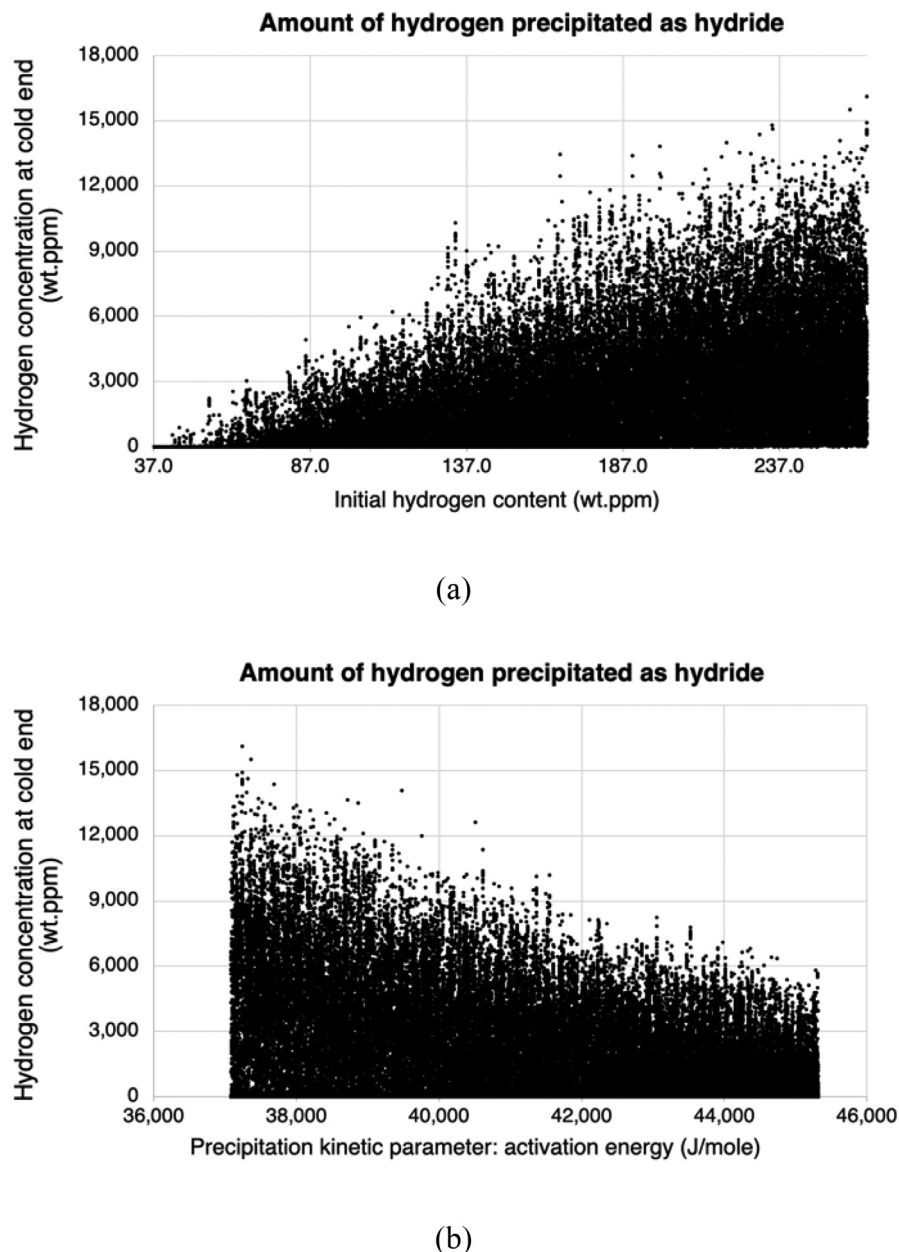


**Fig. 10.** Scatter plot of predicted amount of hydrogen precipitated as hydride with respect to the initial hydrogen content and the activation energy for precipitation kinetic parameter.

initial hydrogen content gave significant effects, for they directly estimated the hydrogen distribution in the sample. Diffusion parameters also provided some effects due to thermal diffusion phenomenon that led to the hydrogen concentrating preferentially at the cold end. The dissolution parameters and the precipitation kinetic parameters were not relevant to the hydrogen in solid solution. On the other hand, Sobol indices computed for the amount of hydrogen precipitated as hydride, as shown in Fig. 9(b), were nearly equal to those for the total hydrogen concentration (See Fig. 7). This implied that the contributions of each input parameter on the total hydrogen concentration at the cold end were determined by how they influenced to the hydrogen precipitated as hydride rather than the hydrogen in solid solution, and thus the sensitivity of total hydrogen concentration was highly dependent

on the precipitation of hydride. To support the explanation, we analyzed scatter plots of both hydrogen concentration in solid solution and amount of hydrogen precipitated as hydride. The scatter plots of amount of hydrogen precipitated as hydride shown in Fig. 10(a)-(b) present similar trends in the prediction with respect to key parameters as those for the total hydrogen concentration (See Fig. 8(a) and (c)). This supported that the prediction of total hydrogen concentration at the cold end was highly dependent on the estimation of how much hydrogen precipitates.

It was noticeable that some extreme combinations of experimental conditions produced predicted hydrogen concentrations outside the physically acceptable range. This is because the developed framework for the sensitivity analysis independently chose the input parameters from each set. Thus, the comparison studies

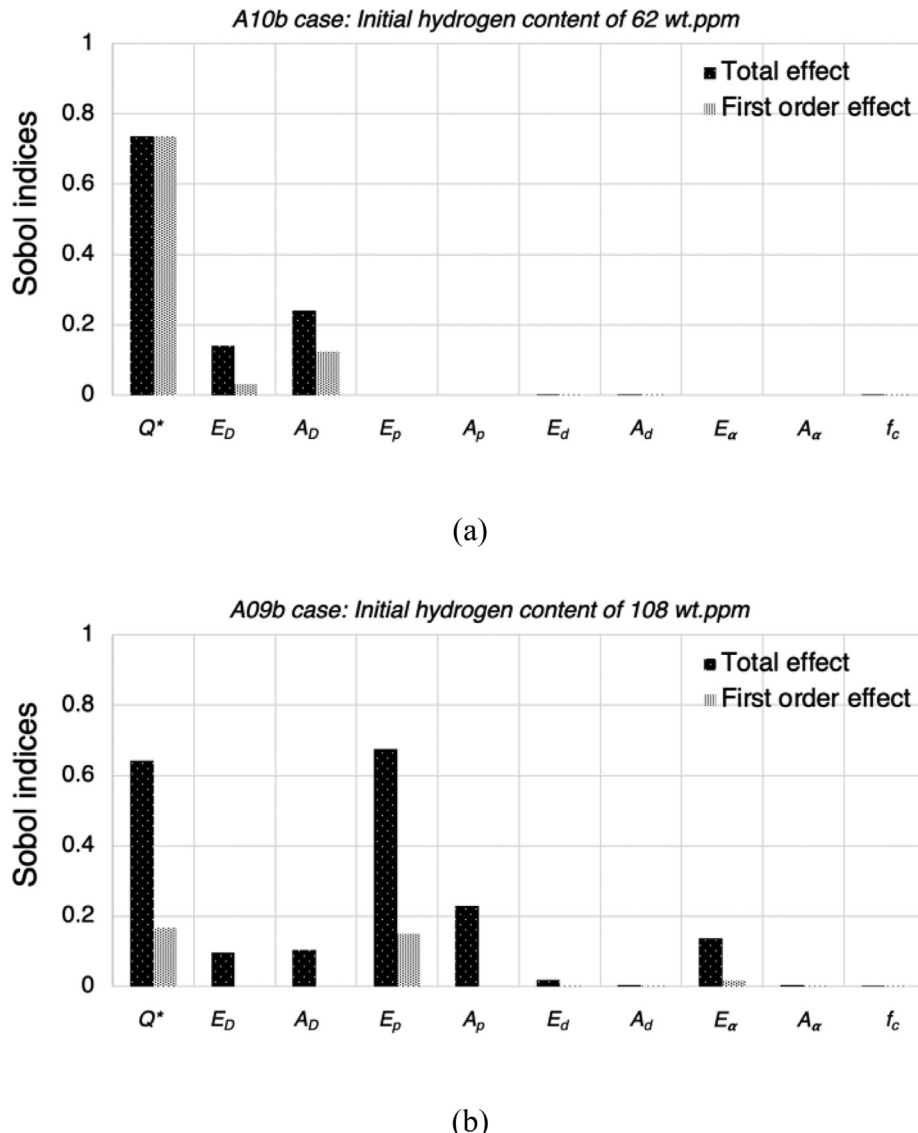


**Fig. 11.** Sobol indices of input parameters computed for cases: (a) A10b case with initial hydrogen content of 62 wt.ppm, (b) A09b case with initial hydrogen content of 108 wt.ppm.

were conducted to reveal the respective impact of environmental conditions on the sensitivity of predicted hydrogen concentration, as presented in the following section.

#### 4.2. Respective impact of environmental conditions to relevant phenomenon

This section presents comparison studies for the specific experimental cases conducted by Kammenzind to reveal the respective impact of environmental conditions on the predicted hydrogen behaviors and their sensitivity with respect to the input parameters. For each comparison study, two experimental cases that have distinct values for the specific environmental condition of interest with other conditions being the same were chosen. Note that all Sobol indices were computed for the total hydrogen concentration at the cold end.

##### 4.2.1. Initial hydrogen content

Fig. 11 presents the Sobol indices of input parameters computed with different initial hydrogen contents. Both A10b and A09b had

the cold end temperature of 589 K, linear temperature gradient of 66.4 K/cm, and annealing time of 32 days. While A10b case had initial hydrogen content of 62 wt.ppm, A09b case had that of 108 wt.ppm. For A10b case where the initial hydrogen content was small, the total hydrogen concentration at the cold end was only dependent on the diffusion parameters. Hardly occurrence of precipitation due to small initial hydrogen content reduced the contribution of precipitation parameters and enhanced that of diffusion parameters. On the other hand, when the initial hydrogen content was large enough to produce the precipitation, the significance of precipitation parameters was enhanced as shown in Fig. 11(b) for A09b case. Therefore, the computed Sobol indices of precipitation parameters involved in both steady-state equilibrium ( $TSS_p$ ,  $TSS_d$ ) and dynamic equilibrium (kinetic parameter) significantly increased.

Fig. 12 presents the scatter plots of predicted hydrogen concentration for each case with respect to the heat of transport that was chosen to show the most distinct trends. At the cold end temperature of 589 K, the minimum and maximum values of  $TSS_p$  were

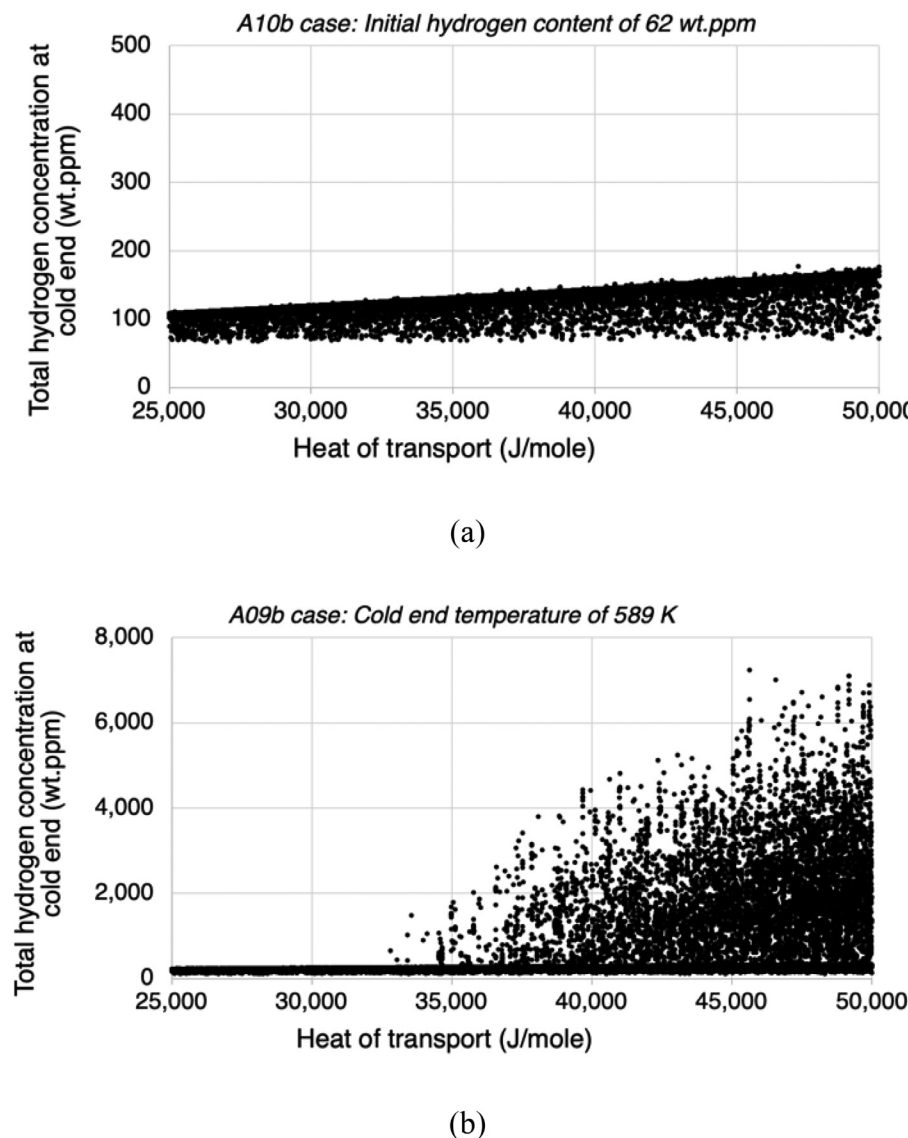


**Fig. 12.** Scatter plot of total hydrogen concentration at the cold end with respect to heat of transport: (a) A10b case, (b) A09b case.

223 and 449 wt.ppm, respectively, and those of  $TSS_d$  were 67 and 171 wt.ppm, respectively. Note that the scales on the y-axis are different between the two scatter plots. When the amount of pre-charged hydrogen was insufficient to drive the precipitation process, as shown in Fig. 12(a), all of the hydrogens remained in solid solution. As the heat of transport increased, the enhanced thermal diffusion by the Soret effect led more hydrogen to be concentrated at the cold end. However, when the amount of initial hydrogen content along the specimen was large enough, precipitation phenomena occurred at the cold end if the heat of transport was large enough to overcome  $TSS_p$  (from  $Q^* = \sim 35,000$  J/mole in Fig. 12(b)). Once precipitation occurred, the contribution of hydrides amount precipitated to the predicted amount of total hydrogen at the cold end began to increase. As more hydrogen was likely to precipitate as hydride at the cold end (increasing  $Q^*$  in Fig. 12(b)), variation in total hydrogen amount predicted by BISON code became larger, indicating the prediction was more sensitive to input parameters. In other words, when large amount of hydrogen is expected to precipitate, the uncertainty in the prediction of hydrogen behavior will increase. Since the initial hydrogen content

gave significant effect on the amount of precipitated hydride, we conclude that the increase in initial hydrogen content could make it more difficult to accurately predict the hydrogen distribution at the end.

#### 4.2.2. Cold end temperature

In this section, Sobol indices for two cases, A46 and A09b, with different cold end temperatures are compared. A46 had the cold end temperature of 533 K, linear temperature gradient of 66.8 K/cm, annealing time of 77 days, and initial hydrogen content of 101 wt.ppm, while A09b had 589 K, 66.4 K/cm, 32 days, and 108 wt.ppm, respectively. First, the Sobol indices of input parameters were computed from the simulations under the cold end temperature of 533 K and 589 K, as shown in Fig. 13(a) and (b), respectively. When the cold end temperature was low, the precipitation of hydrogen was more likely to occur due to the small  $TSS_p$ . As a result, the precipitation kinetic parameter, which determined the amount of hydrogen precipitated as a hydride, contributed the most to the final hydrogen concentration. However, as the cold end temperature increased, the computed Sobol index of

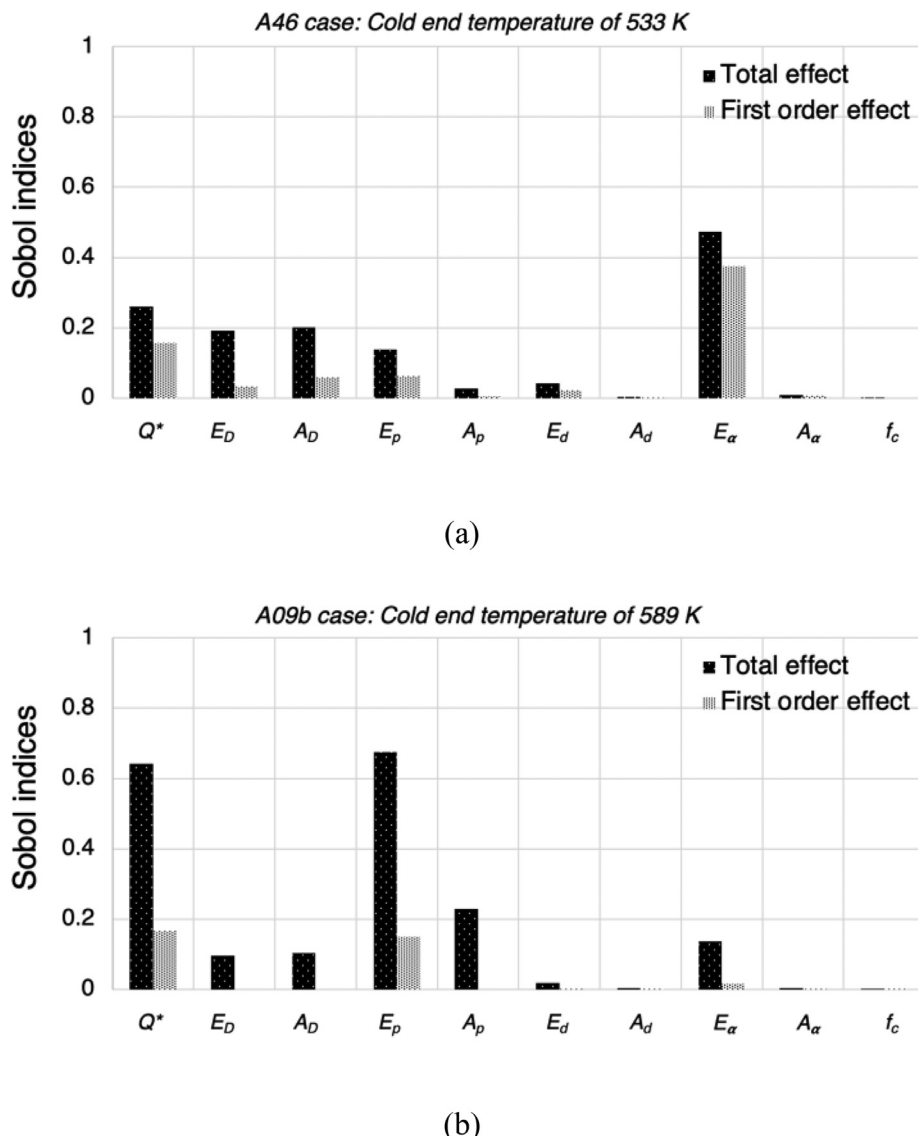


Fig. 13. Sobol indices of input parameters computed for cases: (a) A46 case with cold end temperature of 533 K, (b) A09b case with cold end temperature of 589 K.

precipitation kinetic parameter was significantly reduced. In other words, the precipitation of hydrogen at the cold end was dependent more on  $TSS_p$  than precipitation kinetic parameter, when the cold end temperature is high. This is because the final hydrogen concentration was highly dependent on whether precipitation occurred, when the high temperature raised the  $TSS_p$  value at the cold end. Furthermore, once the  $TSS_p$  was reached, the precipitation occurred rapidly due to high kinetic parameter at higher temperature. Thus, the precipitation was effectively controlled by the  $TSS_p$ , and this led to the lower sensitivity to the kinetic parameter than to the  $TSS_p$ .

Scatter plots of predicted hydrogen concentration, as shown in Fig. 14, supported the above explanation that the high temperature made it hard to exceed  $TSS_p$  at the cold end where precipitation took place. While the predicted hydrogen was scattered for A46 case with lower cold end temperature as shown in Fig. 14(a), there was a threshold behavior in the predicted hydrogen concentration as a function of the activation energy of  $TSS_p$  for A09b case with higher cold end temperature, as presented in Fig. 14(b). And the rapid increase in the predicted hydrogen concentration after

the threshold point indicated the vigorous precipitation driven by high kinetic parameter described above. In summary, low temperature condition favored occurrence of hydrogen precipitation, and this resulted in large scattering of prediction of final hydrogen concentration. On the other hand, prediction of hydrogen under high temperature produced large uncertainties only within the range where the diffusing hydrogen in solid solution overcame the  $TSS_p$  and thus led to the rapid precipitation phenomenon.

#### 4.2.3. Linear temperature gradient

Comparison of Sobol indices computed for cases with different linear temperature gradients is presented in Fig. 15. A26a had the cold end temperature of 533 K, linear temperature gradient of 66.8 K/cm, annealing time of 27 days, and initial hydrogen content of 48 wt.ppm, while A26b had 533 K, 88.8 K/cm, 54 days, and 47 wt.ppm, respectively. The results revealed that the contributions of diffusion parameters and  $TSS_p$  were weakened as the temperature gradient increased, and the Sobol indices for the total effect of the heat of transport and precipitation kinetic parameter remained the same. The strong thermal diffusion of hydrogen toward the cold

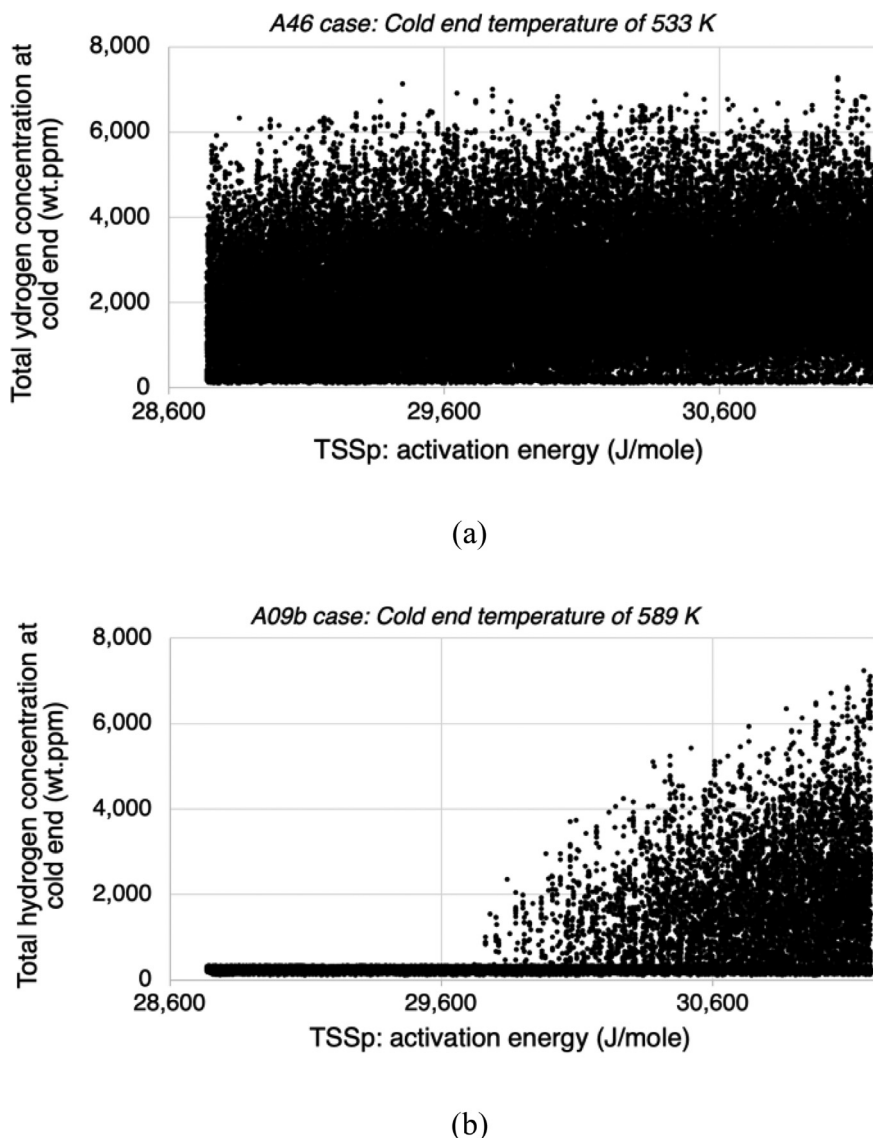


**Fig. 14.** Scatter plot of total hydrogen concentration at the cold end with respect to activation energy of TSS<sub>p</sub>: (a) A46 case, (b) A09b case.

end, driven by the large temperature gradient, led to more hydrogen to accumulate. This made the hydrogen concentration at the cold end easily overcame the threshold of precipitation. This reduced the contribution of TSS<sub>p</sub>, while keeping that of the heat of transport. Note that the Sobol indices for the first order effect of the heat of transport and the activation energy for precipitation kinetic parameter significantly increased as the temperature gradient increased. This indicated that the strong Soret effect reduced the interactive effects among the parameters, and at the same time, enhanced the independent effects of those two parameters.

Scatter plots of predicted hydrogen shown in Fig. 16 present the occurrence of precipitation of hydride at lower value of the heat of transport for A26b case where the temperature gradient is larger. For A26a case, the heat of transport over ~35,000 J/mole is needed to proceed the precipitation, while only about 27,500 J/mole of the heat of transport was enough to produce precipitated hydride at the temperature gradient of 88.8 K/cm as shown in Fig. 16(b). Aforementioned description that the precipitated hydrogen produced large uncertainty in the prediction, accounted for more scat-

tered points at the large temperature gradient case where the precipitation process easily occurred.

#### 4.2.4. Annealing time

Fig. 17 presents the computed Sobol indices of input parameters for two cases annealed over the different periods of time. A10a had the cold end temperature of 589 K, linear temperature gradient of 66.4 K/cm, annealing time of 15 days, and initial hydrogen content of 64 wt.ppm, while A26b had 589 K, 66.4 K/cm, 32 days, and 62 wt.ppm, respectively. While only diffusion parameters contributed to the final prediction of hydrogen for both cases, their Sobol indices were slightly different from each other. The sum of Sobol indices for the total effect of the diffusion coefficient were comparable to the Sobol index of the heat of transport for the low annealing time case. When the sample was exposed to the temperature gradient for the long-time case, the heat of transport dominated the prediction of hydrogen concentration. This is because the strong thermal diffusion due to the linear temperature gradi-

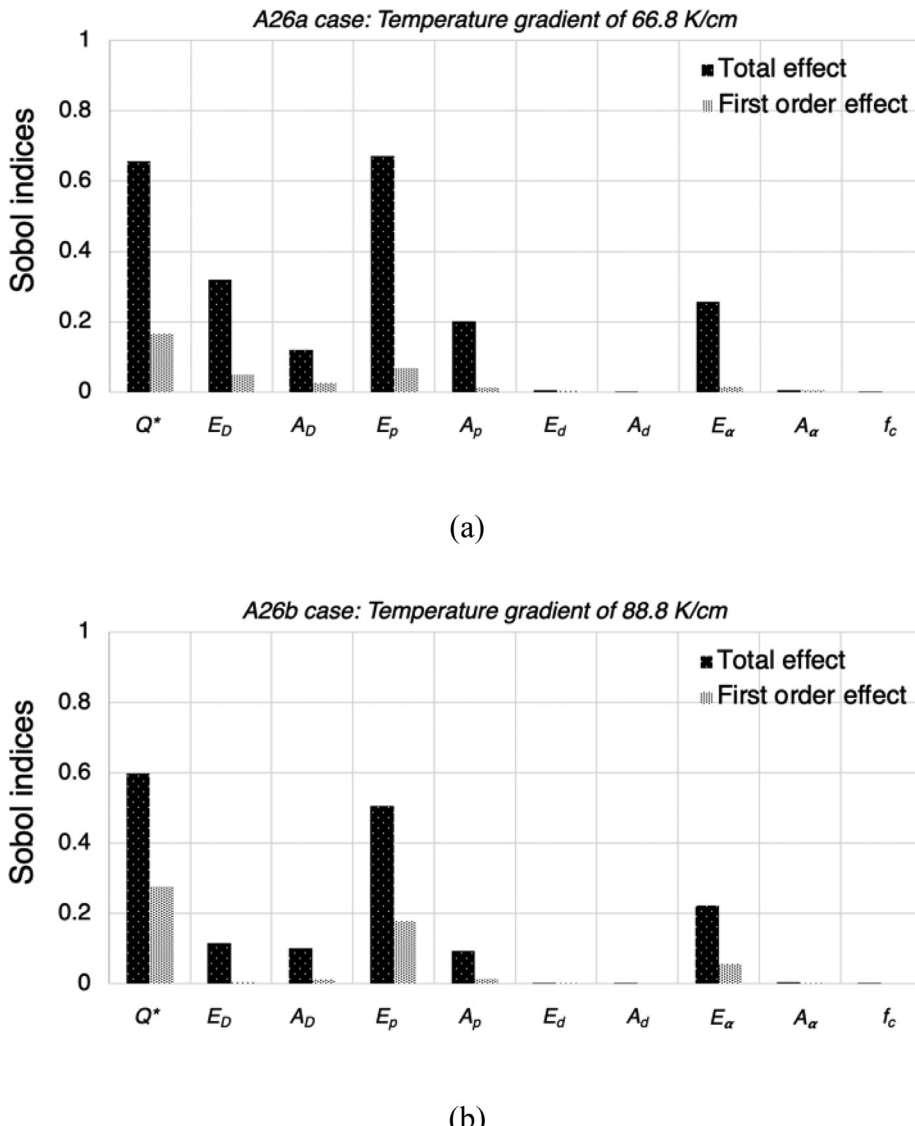


**Fig. 15.** Sobol indices of input parameters computed for cases: (a) A26a case with temperature gradient of 66.8 K/cm, (b) A26b case with temperature gradient of 88.8 K/cm.

ent lasted for the long time, and thus importance of the heat of transport increased.

Fig. 18 presents scatter plots of predicted hydrogen concentration at the cold end between the two cases. The maximum variations in the predicted hydrogen concentration generated from the respective case were nearly the same. This indicated that the annealing time had little influence on the uncertainty in the prediction, for the fast equilibrium in the hydrogen diffusion behavior was achieved in the considered experimental conditions. Note that the relatively high cold end temperature (589 K for both cases) led to all the hydrogen remaining in solid solution over the entire range of the heat of transport

#### 4.3. Optimization study for best-predictive hydrogen model

This section presents the optimization study using the results from the Sobol sensitivity analysis to improve the accuracy of predictive model for the hydrogen distribution in BISON code. We used an approach consistent with the literature [33]. To develop an optimized set of BISON predictions, we used a global stepping

algorithm with a local minimizer at each step [34]. The basin-hopping method [60] was used for the global optimization method in this study. The basin-hopping method has been shown to be useful for complex nonlinear optimization problems with multiple ranges of variables [61]. The basin-hopping optimization is composed of three main features at each iterative step: producing random perturbation of the coordinates, finding local minimum, choosing to accept or reject the new coordinates based on the minimized function value. The acceptance test we used is the standard Metropolis Hastings algorithm, as part of the Markov chain Monte Carlo (MCMC) algorithms [62].

The RMSE was calculated to assess the accuracy of the model predictions [63]. RMSE always has a positive value, and approaching a value of zero indicates an improving prediction of hydrogen distribution in comparison with the experimental results. The studies presented in Section 4.3 aims to answer two questions: (1) whether a single set of input parameters that can accurately predict the hydrogen distributions from various cases exists or not, (2) if not, what parameters should be investigated and how their ranges should be adjusted to enhance the accuracy of prediction.

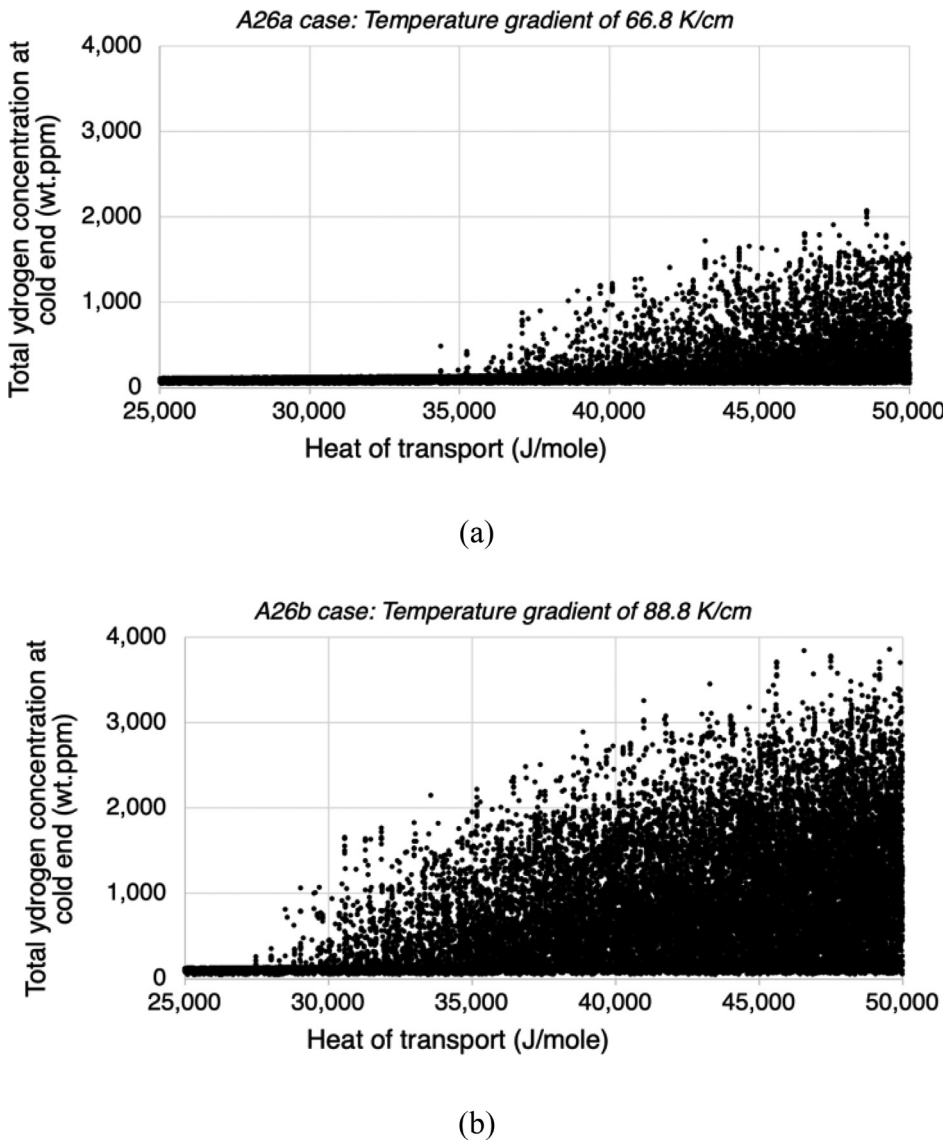


**Fig. 16.** Scatter plot of total hydrogen concentration at the cold end with respect to heat of transport: (a) A26a case, (b) A26b case.

**Table II**

Experimental conditions for chosen cases and their measured heat of transport values.

Cases	Annealing Time [day]	Cold end Temp. [K]	Hot end Temp. [K]	Initial hydrogen content [wt.ppm]	Measured $Q^*$ [J/mole]
A09b case	32	589	755	108	33581
A46 case	77	533	700	101	23200
A10a case	15	589	755	64	30055
A45 case	77	533	700	85	29185

To answer these questions, we chose several experimental cases and found certain ranges of key input parameters that minimized the RMSE between BISON predictions and the experimental data. The experimental cases chosen for this study are summarized in **Table II** including the measured heat of transport values for respective cases. The variation ranges for input parameters were same as those listed in **Table I**, while that for heat or transport was set to  $\pm 20\%$  from measured value of each case.

Based on the sensitivity analysis results, we chose significant parameters for A09b case which have Sobol indices larger than

0.1 (See **Fig. 12(b)**): heat of transport, activation energy and pre-exponential coefficient for diffusion coefficient, activation energy and pre-exponential coefficient for  $TSS_p$ , activation energy for precipitation kinetic parameter. Among the predictions made by BISON code using a range of chosen parameters, those less than 20 % in RMSE value are plotted with the experimental data, as shown in **Fig. 19**. Note that the error of 20 % came from the maximum uncertainty in measurement of the heat of transport in Kammenzind's experiment [48], and the error bars in **Fig. 19** indicate  $\pm 20\%$  from the measured values in the experiments. It was found that

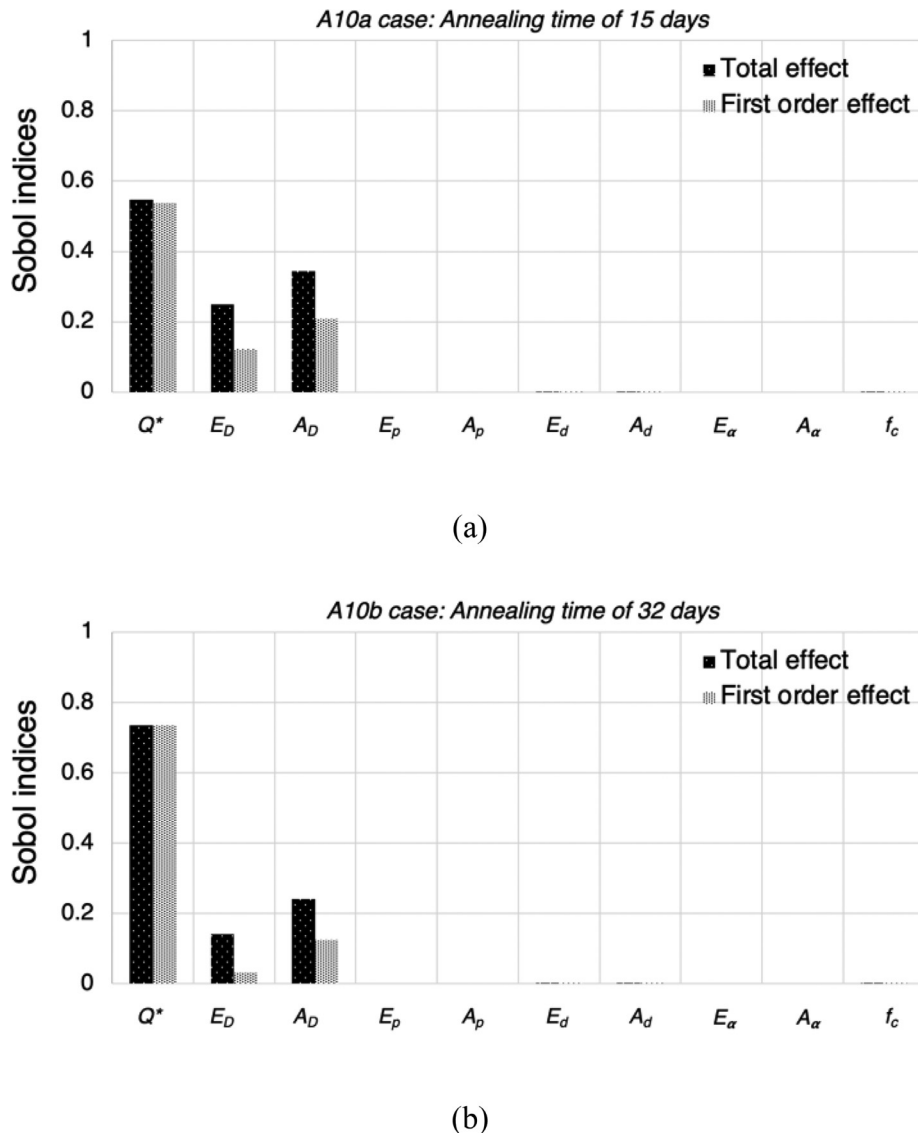


**Fig. 17.** Sobol indices of input parameters computed for cases: (a) A10a with annealing time of 15 days, (b) A10b with annealing time of 32 days.

the discrepancy between the predictions and measured values was the largest for results at the cold end, as expected.

Fig. 20(a)-(c) present more detailed evidence on the calibrated sets of parameters that minimize the RMSE. Note that error bar in y-axis indicates total hydrogen concentration at cold end predicted within  $\pm 20\%$  from experimental data, and the red area represents the range of each parameter. The scatter plots of predictions in Fig. 20(a) indicated that total hydrogen concentration at the cold end was accurately predicted when the heat of transport was large. Furthermore, Fig. 20(b) and (c) present accurate prediction of hydrogen distribution was made in the range of high activation energy and low pre-exponential coefficient of TSS<sub>p</sub>, which provided small TSS<sub>p</sub>. Large heat of transport and small TSS<sub>p</sub> imply enhanced Soret effect and low threshold of which combination led to precipitation more likely to occur. From this result, we assumed that the BISON simulations produced accurate hydrogen predictions when the sets of parametric ranges were shifted to enable more precipitation to occur at the cold end. Other cases with different conditions were analyzed using same method to support the explanation.

Using the same approach, the prediction less than 20 % in RMSE value for A46 case where more precipitated hydrogen were expected (See Fig. 14(a)) were plotted with the experimental data shown in Fig. 21. Steep hydrogen distribution produced some discrepancy at the point next to the cold end, but still that at the left end point contributes the most to the RMSE value. The small TSS<sub>p</sub> due to low temperature allowed the hydrogen in solid solution to be more likely to precipitate as hydrides. This made the final hydrogen concentration at the cold end easily reached the value measured from the experiments. Fig. 22 shows that the number of predictions less than 20 % in RMSE value is larger for A46 case compared to that for A09b case. The scatters plots in Fig. 22(a) and (b) present more data points are made within 20 % of error and they spread to large area in the range of each parameter. This indicates the accuracy of prediction become insensitive to sets of parametric ranges when large precipitation of hydride is expected with any values of input parameters, and this is consistent with the assumption made from A09b case.

Lastly, the optimization study for A10a case, where the precipitation process at the cold end hardly occurred (See Fig. 18(a)), was

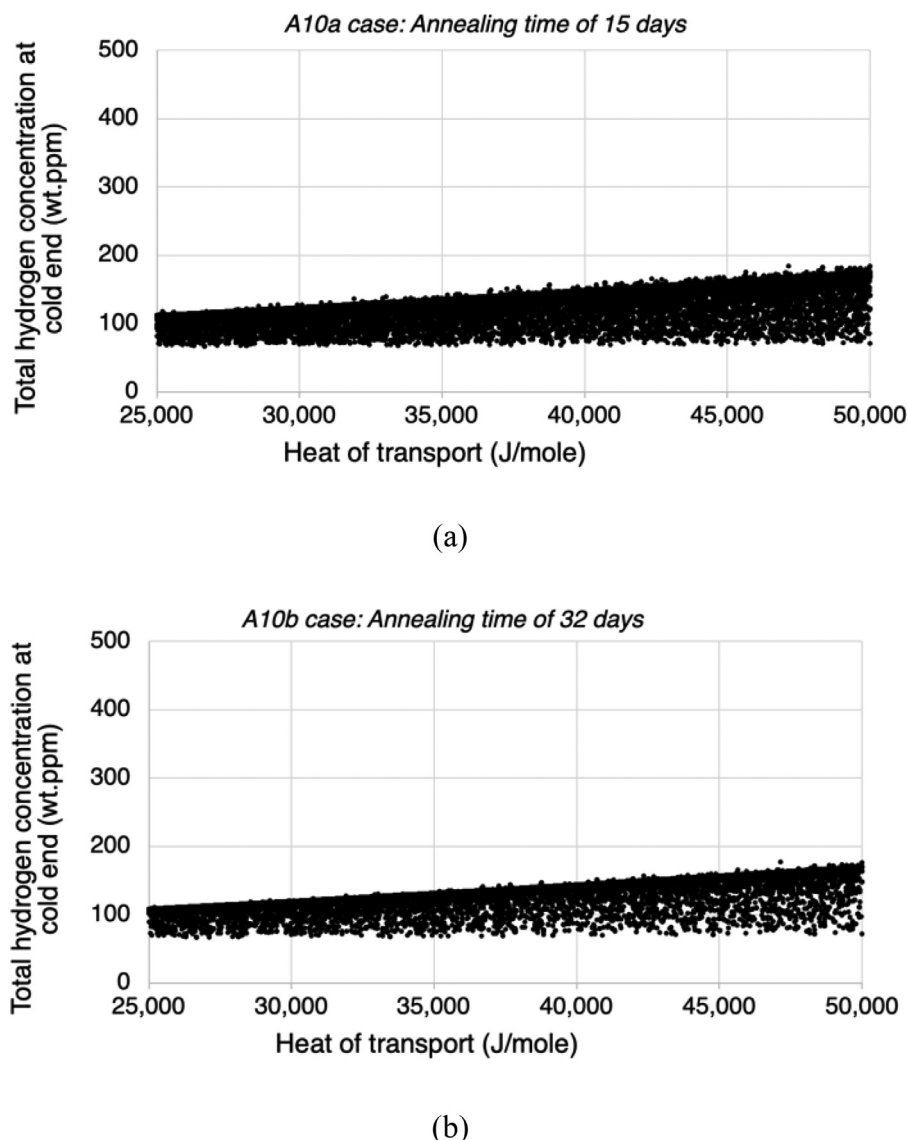


**Fig. 18.** Scatter plot of total hydrogen concentration at the cold end with respect to heat of transport: (a) A10a case, (b) A10b case.

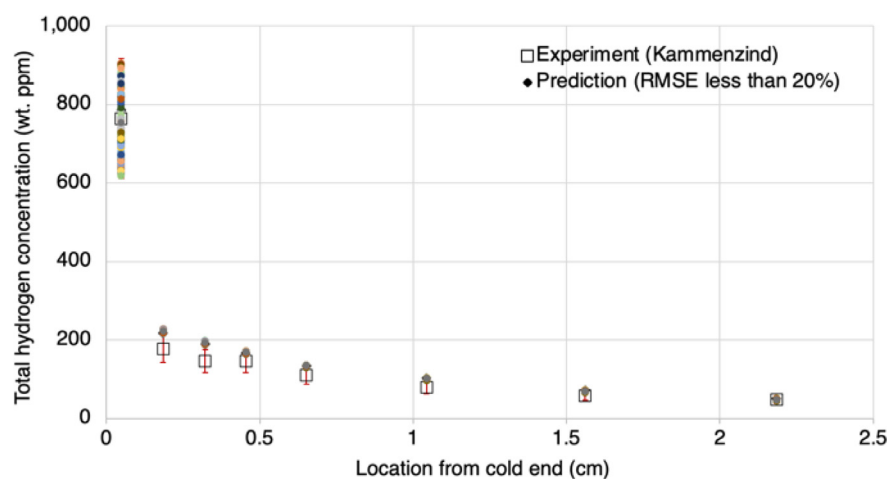


**Fig. 19.** Plots of predicted hydrogen distributions less than 20 % of RMSE for A09b case.

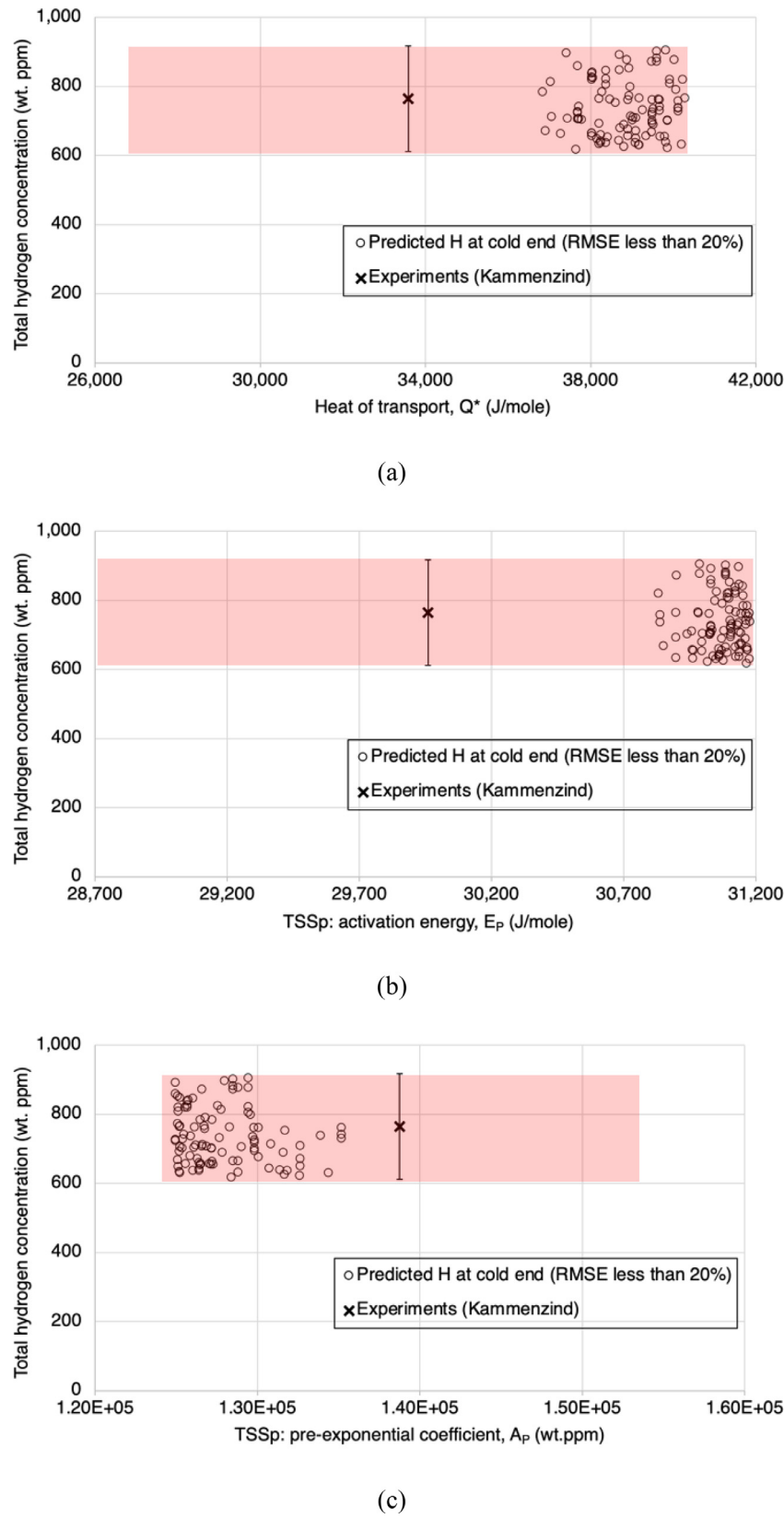


**Fig. 20.** Scatter plots of total hydrogen concentrations at the cold end within 20 % of the RMSE with respect to: (a) heat of transport, (b) TSS<sub>P</sub>: activation energy, (c) TSS<sub>P</sub>: pre-exponential coefficient.

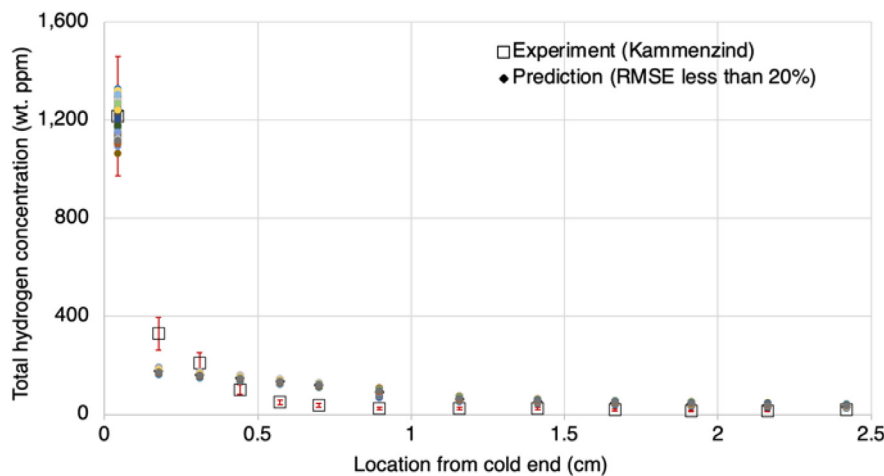


**Fig. 21.** Plots of predicted hydrogen distributions less than 20% of RMSE for A46 case.

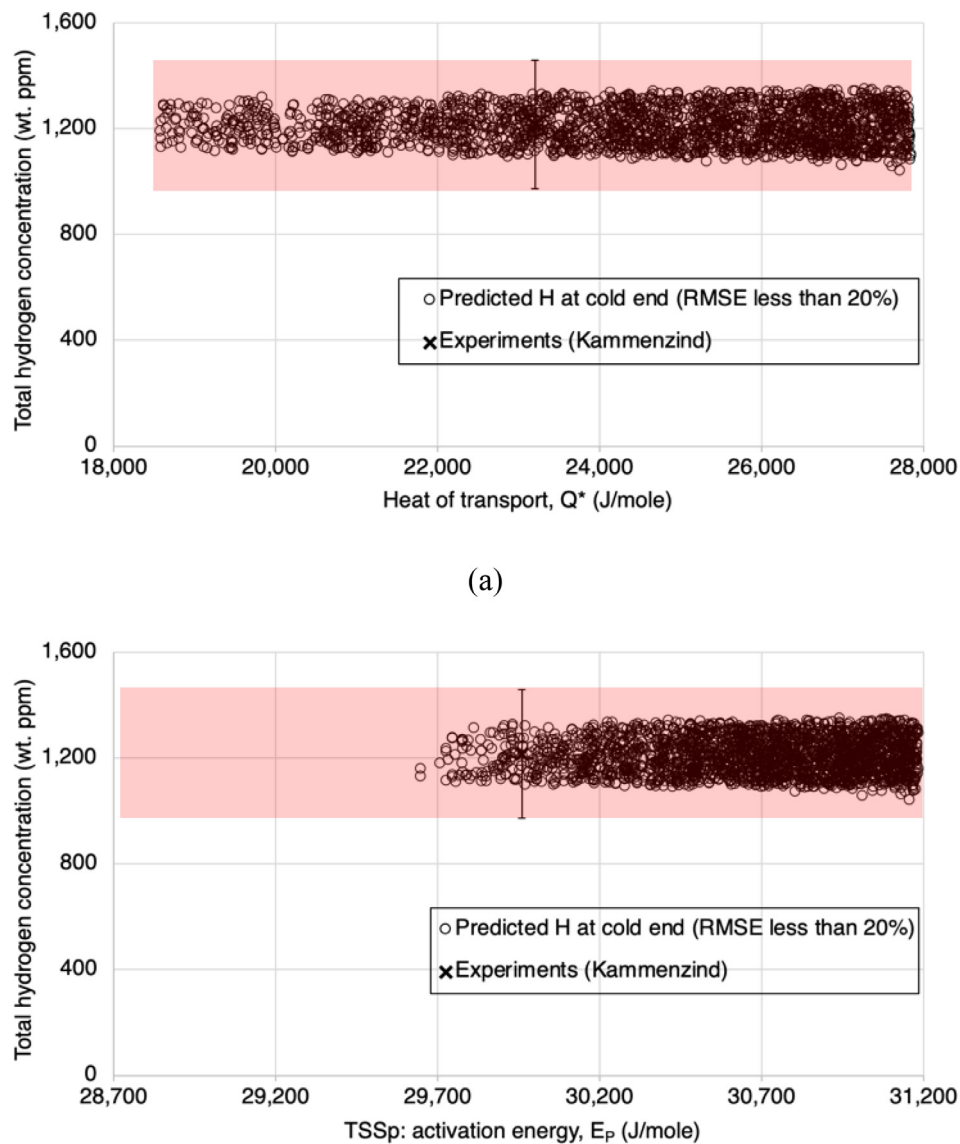


**Fig. 22.** Scatter plots of total hydrogen concentrations at the cold end within 20 % of the RMSE for A46 case, with respect to: (a) heat of transport, (b) TSS<sub>p</sub>: activation energy.

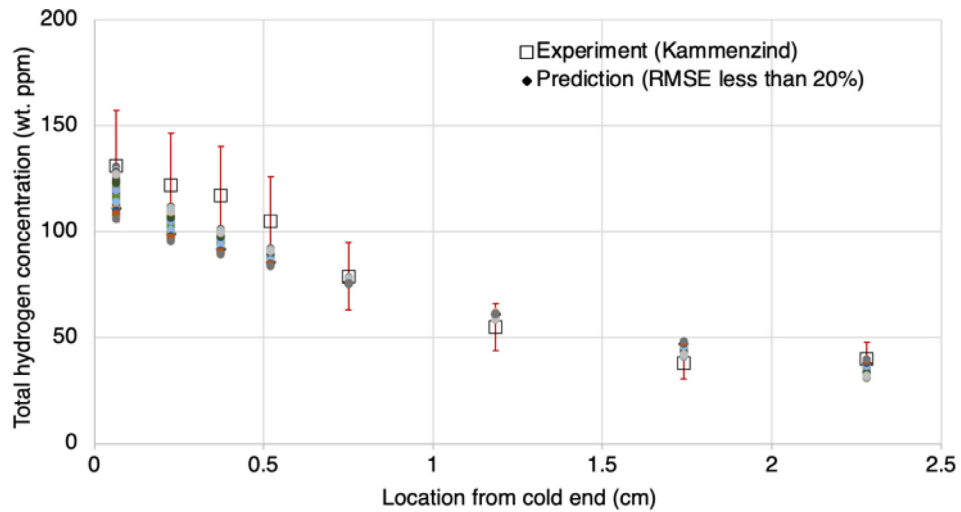


**Fig. 23.** Plots of predicted hydrogen distributions less than 20% of RMSE for A10a case.

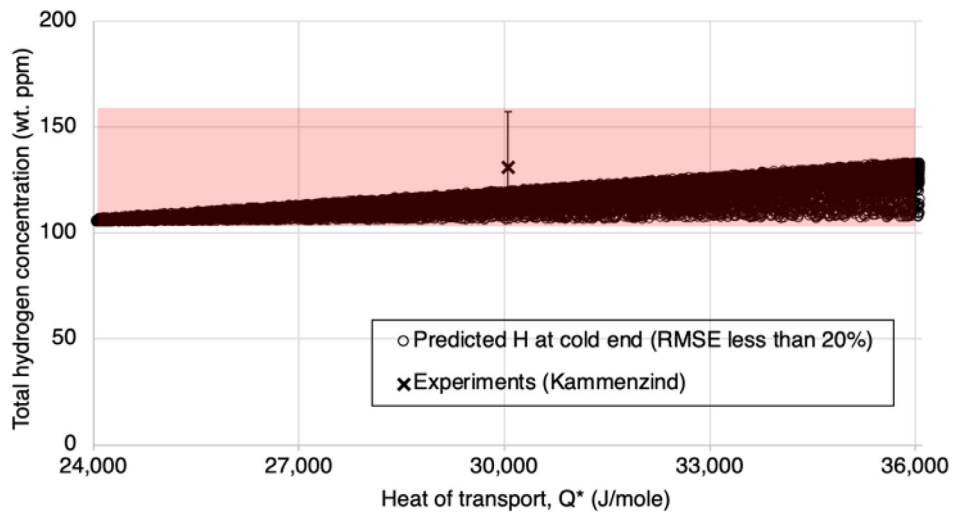


**Fig. 24.** Scatter plots of total hydrogen concentrations at the cold end within 20 % of the RMSE for A10a case, with respect to heat of transport.

conducted. Fig. 23 presents the predictions of hydrogen concentration less than 20 % in the RMSE for A10a case plotted with the experimental data, and Fig. 24 shows scatters of those with respect to heat of transport. Most of the predictions were accurate, and the gradual hydrogen distribution produced small discrepancy along the sample. This is because the final hydrogen concentrations were equivalent to those in the solid solution as precipitation did not occur, and the sensitivity of hydrogen in solid solution was found to be small. However, Fig. 24 represents that strong thermal diffusion driven by large heat of transport resulted in the high concentration of hydrogen at the cold end, and made it be close to the measured value. Therefore, the thermal diffusion of hydrogen was another important process whose representation in the current hydrogen model needed to be improved to achieve accurate prediction.

The calibrated set of parametric ranges, which enhanced diffusion toward the cold end and precipitation of hydrogen at that point, was applied to A45 case to verify that the optimized windows for the parameters led to the best prediction. Note that only the range of higher activation energy for TSS<sub>p</sub> and lower activation energy for diffusion coefficient was considered in the study

for A45 case, as shown in Fig. 25(a) and (b). The scatter plots indicated that most of the predictions were given within 20 % of the RMSE value, and this represented high accuracy of hydrogen predictive model when using the optimized set of parametric ranges. Furthermore, Fig. 25(c) presents little sensitivity of the prediction with respect to the heat of transport, and infers the uncertainty in the estimation of heat of transport no longer influences that in the BISON simulation for the hydrogen distribution. Therefore, it was verified that the use of Sobol sensitivity analysis resulted to evaluate the calibrated set of parameters and its application to the specific cases reduced the overall uncertainties and enhanced the accuracy of the model.

#### 4.4. Sensitivity analysis of benchmarking experiments

The sensitivity and uncertainty analysis used in this study was applied to calibrate the ongoing benchmarking experiments conducted by University of Michigan within the scope of the project. For the BISON simulations of ongoing experiments, the sample described in Section 2.2 was modeled with linear temperature gradient. The 40 mesh elements were split evenly throughout

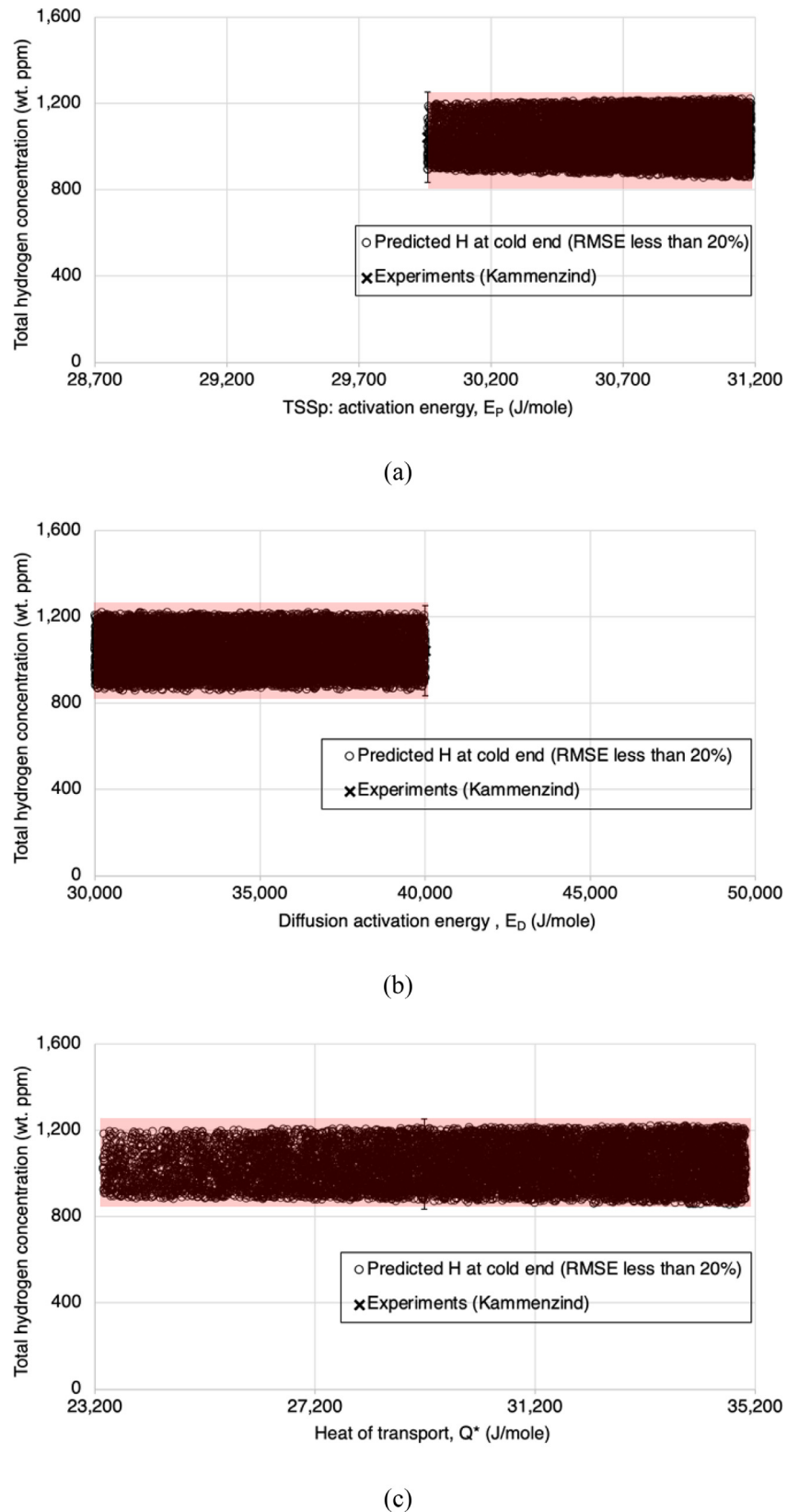


**Fig. 25.** Scatter plots of total hydrogen concentrations at the cold end within 20 % of the RMSE for A45 case, with respect to: (a) activation energy for TSSp, (b) activation energy for diffusion coefficient, (c) heat of transport.

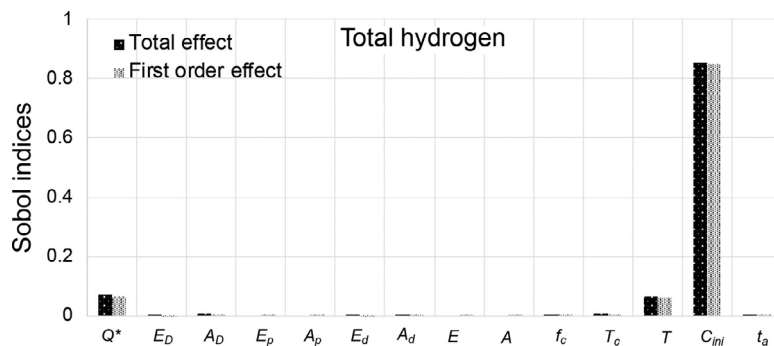


**Fig. 26.** Sobol indices of input parameters for the total hydrogen content at the cold end of specimen in the benchmarking experiments.

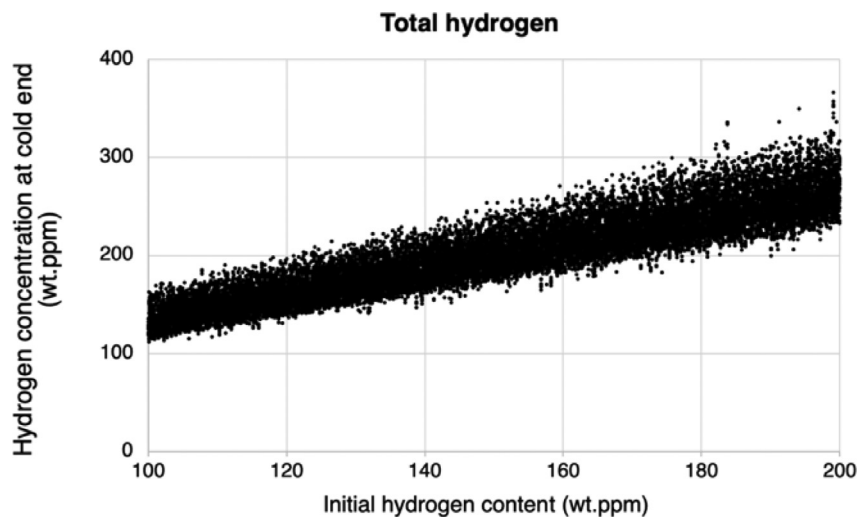


**Fig. 27.** Scatters plot of total hydrogen concentration at the cold end with respect to the initial hydride content in benchmarking experiments.

**Table III**

Adjusted variation range of experimental parameters for the benchmarking experiments.

Parameter	Unit	Lower bound	Upper bound
Cold end temperature, $T_c$	K	670	750
Temperature gradient, $\Delta T$	K/cm	20	40
Initial hydrogen content, $C_{ini}$	wt. ppm	100	200
Annealing time, $t_a$	day	25	35

the geometry, initial hydrogen concentration was equally assigned to each element at the beginning of simulations, and the simulations matched the time for the experiment anneals. **Table III** presents the experimental conditions designed in this series of experiments while variation range of model parameters remains same.

When the experimental conditions were replaced with those from benchmarking experiments, the impacts of all the model parameters were suppressed except for heat of transport, as shown in **Fig. 26**. It indicated that only heat of transport matters in those conditions, or we could evaluate solely the effect of heat of transport from the experiments. It is desirable because the experimental studies aim to evaluate heat of transport for the improvement of hydrogen model. The effect of cold end temperature was also reduced while the effect of temperature gradient was enhanced. It came from the increased minimum temperature over the specimen that suppressed the precipitation and dissolution dynamics during annealing. This could account for the enhanced effect of temper-

ature gradient, as the hydrogen diffusion in solid solution became dominant physics in such high temperature condition. As shown in **Fig. 27**, one can still find the strong linear correlation between the predicted hydrogen and the initial hydrogen content. However, the adjusted experimental conditions led to all the predictions place within the physically acceptable range, and narrowed the absolute variations that implied the reduction of overall uncertainties associated with the experiments. The following studies are focused on the calibration of specific test conditions.

The Sobol indices computed for the benchmarking experiments always represented the significant contributions of diffusion parameters on the predicted hydrogen concentration, as shown in **Fig. 28**. By comparing the environmental conditions of historical experiments, the small temperature gradient from benchmarking experiments was the major attribution to the results that represented less precipitation of hydrogen at the cold end. Since the highest concentration of hydrogen at the cold end was a result from the Soret effect driven by a linear temperature gradient, it was obvious that the small temperature gradient led to less hydrogen diffusion toward the cold end. Overall, the dominance of diffusion phenomena for the hydrogen in solid solution within the hydrogen migration and redistribution model was emphasized in benchmarking experiments. This gives advantages in evaluating the heat of transport, which is an objective the benchmarking experiments pursue. The conclusion given here is that the sensitivity and uncertainty method developed in this study is capable of informing the appropriate envelop of experimental test matrix and verifying the adequacy of the experiments.

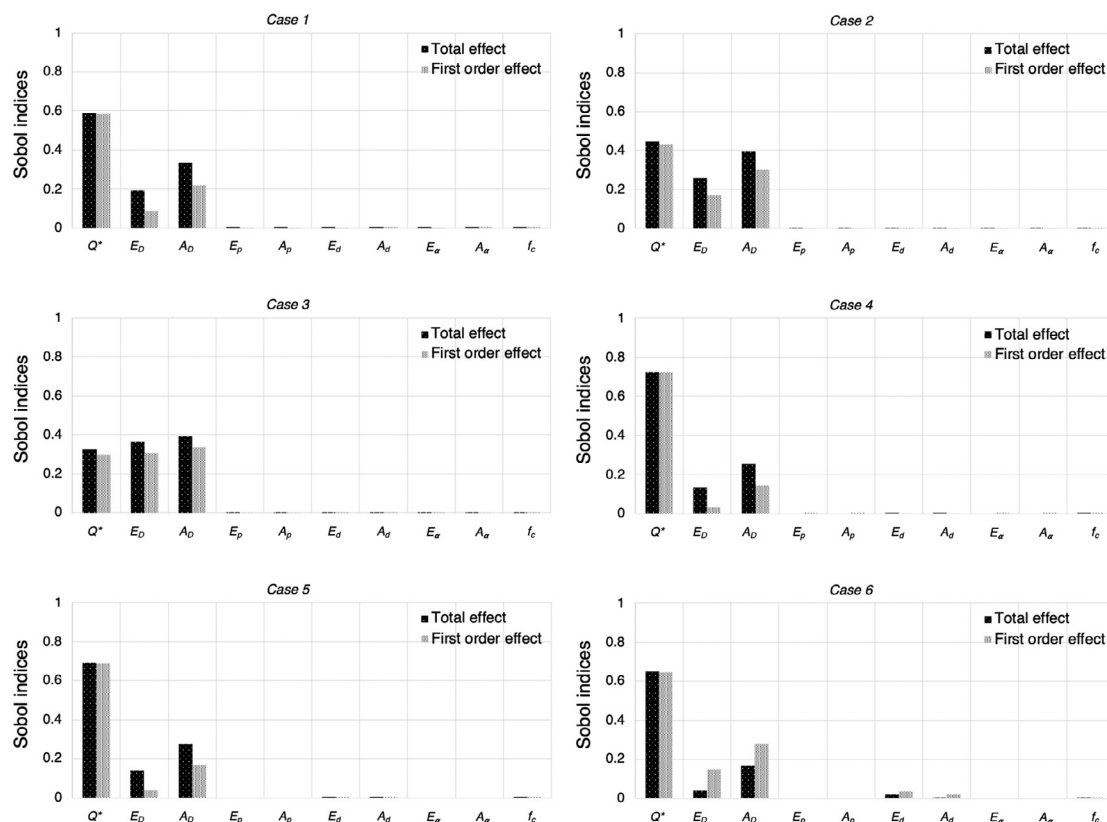


**Fig. 28.** Computed Sobol indices of key input parameters for the predicted hydrogen concentration at the cold end of specimen under environmental conditions from benchmarking experiments.

## 5. Conclusion

The formation of hydrides in nuclear fuel cladding, a result of an excess of hydrogen picked up by the cladding during service, can significantly affect cladding integrity, in particular, during fuel storage and transportation events. To enhance our understanding of hydrogen distribution inside the cladding, a sensitivity and uncertainty analysis of a hydrogen predictive model using the Sobol sensitivity technique is conducted. In particular, the present paper provides improved characterization of the key input parameters involved in the model in regard to the predicted hydrogen distribution under linear temperature gradients, thereby, revealing the impacts of environmental conditions on it.

The predicted total hydrogen concentration at the cold end is chosen as the operating FoM for this study, and the set of input parameters includes model parameters related to the hydrogen migration and redistribution model and experimental parameters related to the environmental conditions. A Sobol technique, which is a variance-based method, is used for global sensitivity analysis to identify the most influential input parameters. The Sobol sensitivity analysis reveals that the initial hydride content plays a dominant role in the prediction of total hydrogen concentration at the cold end, for the initial hydrogen content directly determines the expected total hydrogen content distributed along the specimen. The cold end temperature has a significant effect as well, producing the second largest Sobol index for first order effect. The diffusion in solid solution and solid solubilities are highly dependent on the temperature profile along the specimen.

Comparative studies for specific experimental cases indicate the respective impact of environmental conditions on the predicted hydrogen behaviors and their sensitivity with respect to the input parameters. Overall, the amount of hydrogen precipitated at the

cold end is the most important factor when estimating the uncertainty in the prediction of hydrogen concentration, and the increase in initial hydrogen content can increase the uncertainty in the predicted hydrogen distribution at the end. Furthermore, the precipitation of hydrogen occurs over the entire range of the heat of transport resulting in large scattering of prediction with low temperature conditions, and high temperature conditions produce large uncertainties where the precipitation easily occurs.

Using sensitivity analysis, an optimization study is performed to improve the accuracy of the predictive model for the hydrogen distribution in the BISON code. A series of calibration studies reveals that the diffusion of hydrogen toward the cold end as well as the precipitation of hydrogen at the cold end are the most important processes in the current hydrogen model. In particular, the BISON simulations produce accurate hydrogen predictions when the sets of parametric ranges are shifted to enable more precipitation to occur at the cold end. The calibrated set of parametric ranges is applied to the following analysis to verify that the optimized windows for the parameters leads to the improved prediction. It reveals high accuracy of hydrogen predictive model when using the optimized set of parametric ranges. Finally, it is verified that the use of Sobol sensitivity analysis results to evaluate the calibrated set of parameters and its application to the specific cases reduce the overall uncertainties and enhance the accuracy of the model.

Lastly, the sensitivity and uncertainty analysis is applied to calibrate the ongoing benchmarking experiments conducted by the University of Michigan. When the experimental conditions were replaced with those from benchmarking experiments, the impacts of all the model parameters were suppressed except for heat of transport. It indicates that solely the effect of heat of transport can be evaluated from the experiments which is the goal of the experimental studies aiming for the improvement of hydrogen model.

The results support that the sensitivity and uncertainty method developed in this study is capable of informing the appropriate envelop of experimental test matrix and verifying the adequacy of the experiments.

The outputs are expected to characterize the various parameters involved in the hydrogen transport model implemented into the BISON code, and improve the understanding of the hydrogen transport behaviors in zirconium-based fuel cladding within a range of expected environmental conditions. In the support of ongoing researches to improve hydrogen predictive model, future work will investigate the contributions of updated features in HNGD model and expand it to more accurately account for hydrogen behavior.

## Declaration of Competing Interest

The authors declare no conflict of interest.

## Acknowledgement

This work was funded by a U.S. Department of Energy Integrated Research Project entitled “Development of a Mechanistic Hydride Behavior Model for Spent Fuel Cladding Storage and Transportation: IRP-FC-1: Modeling of Spent Fuel Cladding in Storage and Transportation Environments”. We gratefully thank Dr. Bruce Kammenzind for providing information about experiments and data.

## References

- [1] T. Alam, et al., A review on the clad failure studies, *Nucl. Eng. Des.* 241 (9) (2011) 3658–3677.
- [2] Lemaignan, C. and A.T. Motta, *Zirconium alloys in nuclear applications. Materials Science and Technology, A Comprehensive Treatment*, ed. B.R.T. Frost. Vol. 10 B. 1994, New York: VCH.
- [3] A.T. Motta, L.-Q. Chen, Hydride formation in Zirconium alloys, *Jom* 64 (12) (2012) 1403–1408.
- [4] T. Fuketa, T. Sugiyama, F. Nagase, Behavior of 60 to 78MWd/kgU PWR fuels under reactivity-initiated accident conditions, *J. Nucl. Sci. Technol.* 43 (9) (2006) 1080–1088.
- [5] J. Brachet, et al., Influence of hydrogen content on the  $\alpha/\beta$  phase transformation temperatures and on the thermal-mechanical behavior of Zy-4, M4 (ZrSnFeV), and M5<sup>TM</sup> (ZrNbO) alloys during the first phase of LOCA transient, *Zirconium in the Nuclear Industry: Thirteenth International Symposium*, ASTM International, West Conshohocken, PA, 2002.
- [6] S. Kass, Hydrogen pickup in various Zirconium alloys during corrosion exposure in high-temperature water and steam, *J. Electrochem. Soc.* 107 (7) (1960) 594–597.
- [7] S. Suman, et al., Effects of hydrogen on thermal creep behaviour of Zircaloy fuel cladding, *J. Nucl. Mater.* 498 (2018) 20–32.
- [8] S. Banerjee, P. Mukhopadhyay, Phase transformations examples from titanium and zirconium alloys, 1st ed., Pergamon, Amsterdam, The Netherlands, 2007.
- [9] A.T. Motta, et al., Hydrogen in zirconium alloys: A review, *J. Nucl. Mater.* 518 (2019) 440–460.
- [10] C.E. Ells, Hydride precipitates in zirconium alloys (A review), *J. Nucl. Mater.* 28 (1968) 129–151.
- [11] J.J. Kearns, Terminal solubility and partitioning of hydrogen in the alpha phase of zirconium, zircaloy-2 and zircaloy-4, *J. Nucl. Mater.* 22 (1967) 292–303.
- [12] R.S. Daum, et al., The influence of a hydrided layer on the fracture of Zircaloy-4 cladding tubes, in: *International Conference on Hydrogen Effects on Material Behaviour and Corrosion Deformation Interactions*, Moran, WY, United States, 2002, pp. 22–26. Sep.
- [13] S. Suman, et al., Hydrogen in Zircaloy: mechanism and its impacts, *Int. J. Hydrog. Energy* 40 (17) (2015) 5976–5994.
- [14] S. Morozumi, et al., Effects of alloying elements and cold work on the redistribution of hydrogen in zirconium under a temperature gradient, *J. Nucl. Mater.* 33 (1969) 261–270.
- [15] B.F. Kammenzind, et al., Hydrogen pickup and redistribution in alpha-annealed zircaloy-4, in: E.R. Bradley, G.P. Sabol (Eds.), *Zirconium in the Nuclear Industry: 11th International Symposium*, ASTM STP1295, ASTM International, West Conshohocken, PA, 1996.
- [16] A. Sawatzky, The diffusion and solubility of hydrogen in the alpha-phase of zircaloy-2, *J. Nucl. Mater.* 2 (1) (1960) 62–68.
- [17] A. Sawatzky, The heat of transport of hydrogen in zirconium alloys, *J. Nucl. Mater.* 9 (3) (1963) 364.
- [18] Sugisaki, M., K. Hashizume, and Y. Hatano, *Estimation of hydrogen redistribution in zircaloy cladding of spent fuel under thermal conditions of dry storage and evaluation of its influence on mechanical properties of the cladding*. 2002, IAEA: Vienna, Austria.
- [19] W. Kiauka, C. van Cuyck, W. Keune, Evidence against amorphous phase formation by the solid state reaction of iron on single-crystal Zr(0001) in ultrahigh vacuum, *Mater. Sci. Eng. B12* (1992) 273–279.
- [20] M. Koiba, et al., in: *Temperature Dependence of Heat of Transport of Hydrogen in Zirconium*, in *Defect and Diffusion Forum*, Trans Tech Publications, Ltd, Jan. 1993, pp. 323–328.
- [21] Y. Choi, et al., Hydride formation by high temperature cathodic hydrogen charging method and its effect on the corrosion behavior of Zircaloy-4 tubes in acid solution, *J. Nucl. Mater.* 256 (1998) 124–130.
- [22] O.F. Courtney, et al., Hydride precipitation kinetics in Zircaloy-4 studied using synchrotron X-ray diffraction, *J. Nucl. Mater.* 461 (2015) 180–185.
- [23] H.S. Hong, S.J. Kim, K.S. Lee, Thermotransport of hydrogen in Zircaloy-4 and modified Zircaloy-4, *J. Nucl. Mater.* 257 (1998) 15–20.
- [24] G. Ostberg, Determination of hydride solubility in alpha phase zirconium, zircaloy-2 and zircaloy-4, *J. Nucl. Mater.* 5 (2) (1962) 208–215.
- [25] P. Vizcaino, A.D. Banchik, J.P. Abriata, Solubility of hydrogen in Zircaloy-4: irradiation induced increase and thermal recovery, *J. Nucl. Mater.* 304 (2002) 96–106.
- [26] E. Lacroix, A.T. Motta, J.D. Almer, Experimental determination of zirconium hydride precipitation and dissolution in zirconium alloy, *J. Nucl. Mater.* 509 (2018) 162–167.
- [27] K. Une, S. Ishimoto, Dissolution and precipitation behavior of hydrides in Zircaloy-2 and high Fe Zircaloy, *J. Nucl. Mater.* 322 (1) (2003) 66–72.
- [28] O. Zanellato, et al., Synchrotron diffraction study of dissolution and precipitation kinetics of hydrides in Zircaloy-4, *J. Nucl. Mater.* 420 (1–3) (2012) 537–547.
- [29] K. Une, S. Ishimoto, Terminal solid solubility of hydrogen in unalloyed zirconium by differential scanning calorimetry, *J. Nucl. Sci. Technol.* 41 (9) (2004) 949–952.
- [30] A. McMinn, E. Darby, J. Schofield, The terminal solid solubility of hydrogen in zirconium alloys, in: G. Sabol, G. Moan (Eds.), *Zirconium in the Nuclear Industry: Twelfth International Symposium*, ASTM International, 2000, pp. 173–195.
- [31] F. Nagase, Hydride behavior in Zircaloy cladding tube during high-temperature transients, *J. Nucl. Mater.* 415 (1) (2011) 117–122.
- [32] M. Billone, et al., *Cladding Embrittlement During Postulated Loss-of-Coolant Accidents*, U.S. Nuclear Regulatory Commission, 2008.
- [33] Z. Aly, et al., Variance-based sensitivity analysis applied to hydrogen migration and redistribution model in Bison. Part I: Simulation of historical experiments, *J. Nucl. Mater.* 524 (2019) 90–100.
- [34] Z. Aly, et al., Variance-based sensitivity analysis applied to the hydrogen migration and redistribution model in Bison. Part II: uncertainty quantification and optimization, *J. Nucl. Mater.* 523 (2019) 478–489.
- [35] D.S. Stafford, Multidimensional simulations of hydrides during fuel rod lifecycle, *J. Nucl. Mater.* 466 (2015) 362–372.
- [36] E. Lacroix, et al., Zirconium hydride precipitation and dissolution kinetics in the hysteresis region in zirconium alloys, *ASTM* (2019) **In press**.
- [37] J.J. Kearns, Diffusion coefficient of hydrogen in alpha zirconium, Zircaloy-2 and Zircaloy-4, *J. Nucl. Mater.* 43 (1972) 330–338.
- [38] B. Kammenzind, et al., The long-range migration of hydrogen through zircaloy in response to tensile and compressive stress gradients, in: *Zirconium in the Nuclear Industry: Twelfth International Symposium*, ASTM International, West Conshohocken, PA, 2000, pp. 196–233.
- [39] M.P. Puls, Review of the thermodynamic basis for models of delayed hydride cracking rate in zirconium alloys, *J. Nucl. Mater.* 393 (2) (2009) 350–367.
- [40] O. Courtney, A.T. Motta, J.D. Hales, Modeling and simulation of hydrogen behavior in Zircaloy-4 fuel cladding, *J. Nucl. Mater.* 452 (1–3) (2014) 311–320.
- [41] D.O. Northwood, U. Kosashii, Hydrides and delayed hydrogen cracking in zirconium and its alloys, *Int. Metals Rev.* 28 (1) (1983) 92–121.
- [42] M.P. Puls, *The Effect of Hydrogen and Hydrides on the Integrity of Zirconium Alloy Components: Delayed Hydride Cracking*, Springer, London, 2014.
- [43] M. Kerr, et al., Observation of growth of a precipitate at a stress concentration by synchrotron X-ray diffraction, *Scr. Mater.* 62 (6) (2010) 341–344.
- [44] Y. Zhang, et al., Homogeneous hydride formation path in  $\alpha$ -Zr: Molecular dynamics simulations with the charge-optimized many-body potential, *Acta Mater.* 111 (2016) 357–365.
- [45] Y. Zhang, et al., Sea surface target detection based on complex ARMA-GARCH processes, *Digit. Signal Process.* 70 (2017) 1–13.
- [46] G.P. Marino, Hydrogen supercharging in Zircaloy, *Mater. Sci. Eng. A* 7 (6) (1971) 335–341.
- [47] F. Passelaigue, et al., Implementation and validation of the hydride nucleation-growth-dissolution (HNGD) model in BISON, *J. Nucl. Mater.* 544 (2021) 152683.
- [48] J.T. Merlin, Experiments In Hydrogen Distribution In Thermal Gradients Calculated Using Bison, Masters paper, in Nuclear Engineering, The Pennsylvania State University, 2019.
- [49] R.L. Williamson, et al., Multidimensional multiphysics simulation of nuclear fuel behavior, *J. Nucl. Mater.* 423 (1–3) (2012) 149–163.
- [50] T. Ikonen, Comparison of global sensitivity analysis methods – Application to fuel behavior modeling, *Nucl. Eng. Des.* 297 (2016) 72–80.
- [51] X. Zheng, et al., An integrated approach to source term uncertainty and sensitivity analyses for nuclear reactor severe accidents, *J. Nucl. Sci. Technol.* 53 (3) (2016) 333–344.
- [52] G. Li, H. Rabitz, Relationship between sensitivity indices defined by variance- and covariance-based methods, *Reliab. Eng. Syst. Saf.* 167 (2017) 136–157.
- [53] I.M. Sobol, Global sensitivity indices for nonlinear mathematical models and their Monte Carlo estimates, *Math. Comput. Simul.* 55 (2001) 271–280.

- [54] A. Saltelli, et al., Variance based sensitivity analysis of model output. Design and estimator for the total sensitivity index, *Comput. Phys. Commun.* 181 (2) (2010) 259–270.
- [55] R. Tang, X. Yang, Dissolution and precipitation behaviors of hydrides in N18, Zry-4 and M5 alloys, *Int. J. Hydrom. Energy* 34 (17) (2009) 7269–7274.
- [56] A. Saltelli, Making best use of model evaluations to compute sensitivity indices, *Comput. Phys. Commun.* 145 (2002) 280–297.
- [57] M. Awad, et al., Convergence of sensitivity analysis methods for evaluating combined influences of model inputs, *Reliab. Eng. Syst. Saf.* 189 (2019) 109–122.
- [58] F. Sarrazin, F. Pianosi, T. Wagener, Global sensitivity analysis of environmental models: convergence and validation, *Environ. Model. Softw.* 79 (2016) 135–152.
- [59] G. Glen, K. Isaacs, Estimating Sobol sensitivity indices using correlations, *Environ. Model. Softw.* 37 (2012) 157–166.
- [60] D.J. Wales, *Energy Landscapes: with Applications to Clusters, Biomolecules and Glasses*, Cambridge University Press, Cambridge, UK, 2003.
- [61] B. Olson, et al., Basin hopping as a general and versatile optimization framework for the characterization of biological macromolecules, *Adv. Artif. Intell.* 2012 (2012) 1–19.
- [62] Z. Li, H.A. Scheraga, Monte Carlo-minimization approach to the multiple-minima problem in protein folding, National Academy of Sciences of the United States of America, 1987.
- [63] R.J. Hyndman, A.B. Koehler, Another look at measures of forecast accuracy, *Int. J. Forecast.* 22 (4) (2006) 679–688.